PERGAMON

J. Mech. Phys. Solids 47 (1999) 2411–2449

JOURNAL OF THE MECHANICS AND PHYSICS OF SOLIDS

The effect of bond strength and loading rate on the conditions governing the attainment of intersonic crack growth along interfaces

A. Needleman[a,*], A.J. Rosakis[b]

[a]*Division of Engineering, Brown University, Providence, RI 02912, USA*
[b]*Division of Engineering and Applied Science, California Institute of Technology, Pasadena, CA 91125, USA*

Received 29 June 1998; received in revised form 6 January 1999

Abstract

Dynamic crack growth along a bimaterial interface under impact shear loading is analyzed numerically. The material on each side of the bond line is characterized by an isotropic hyperelastic constitutive relation. A cohesive surface constitutive relation is also specified that relates the tractions and displacement jumps across the bond line and that allows for the creation of new free surface. The resistance to crack initiation and the crack speed history are predicted without invoking any additional failure criterion. Full finite strain transient analyses are carried out. A plane strain model of the configuration used in experiments of Rosakis and co-workers is analyzed. Calculations are carried out for parameters characterizing a steel-PMMA bimaterial. For a sufficiently low impact velocity, the crack speed increases smoothly to the PMMA Rayleigh wave speed, whereas above a sharply defined transition impact velocity, the crack speed reaches a value somewhat less than the PMMA dilational wave speed. This high speed crack growth is associated with multiple crack face contact, separated by discrete micro-crack like openings behind the main shear crack. The calculations reproduce, at least qualitatively, the type of crack speed histories and crack tip fields seen in the experiments. They are also consistent with optical observations of finite multi-site contact occurring at intersonic crack speeds.

Keywords: A. Dynamic fracture; B. Elastic material; C. Finite elements; Interfacial crack

* Corresponding author. Tel.: +1-401-863-2863; fax: +1-401-863-1157.
E-mail address: needle@engin.brown.edu (A. Needleman)

0022-5096/99/$ - see front matter
PII: S0022-5096(99)00012-5

1. Introduction

The term intersonic is used to refer to interfacial crack propagation at speeds between the shear wave and longitudinal wave speeds of the more compliant material of the bimaterial system. Correspondingly, the terms subsonic and supersonic refer, respectively, to crack propagation at speeds below and above all characteristic wave speeds of the more compliant material.

Until quite recently research in the area of dynamic interfacial fracture mechanics has been focused primarily on the study of the subsonic regime of dynamic crack growth. The first experimental evidence of high speed, subsonic, crack growth in bimaterial interfaces was presented by Tippur and Rosakis (1991) who performed low impact speed drop weight tower experiments on aluminum-PMMA specimens and found that crack tip speeds easily approached the smaller of the two Rayleigh wave speeds, suggesting the possibility of high velocity intersonic crack growth. Motivated by these experimental observations, a number of theoretical and numerical investigations were carried out to address some of the fundamental issues related to the fracture of bimaterial interfaces in the subsonic regime (Yang et al., 1991; Liu et al., 1993; Deng, 1993; Nakamura, 1991; Lo et al., 1994; Xu and Needleman, 1995, 1996).

It should be emphasized that in homogeneous (monolithic) materials which contain no preferable weak crack growth paths, and when the loading is not applied directly to the crack faces, observations of crack growth speeds greater than the shear wave speed are non-existent. For remotely loaded cracks in monolithic materials, energy considerations make it impossible for the crack tip speed to exceed the Rayleigh wave speed of the material (Broberg, 1960; Freund, 1990; Washabaugh and Knauss, 1994). There have, however, been experimental observations of intersonic or supersonic crack tip speeds for crack growth along weak crystal planes in anisotropic single crystals of potassium chloride, where the crack faces were loaded by laser induced expanding plasma (Winkler et al., 1970; Curran et al., 1970). At a totally different length scale, indirect observation of intersonic shear rupture has also been reported for crustal earthquakes (Archuleta, 1982). Here the loading is primarily shear dominated and the material is not strictly monolithic since preferable weak crack growth paths exist in the form of fault lines. These observations have motivated extensive theoretical work in the area of high-speed shear fracture in homogeneous materials. Studies have been conducted with seismological applications in mind and include the work of Burridge (1973), Andrews (1976), Burridge et al. (1979), Freund (1979), Broberg (1985, 1989), Georgiadis (1986), Bykovtsev and Kramarovskii (1989) and Aleksandrov and Smetanin (1990).

The situation in bimaterials (containing weak interfaces) is quite different from that in homogeneous monolithic solids and may share general features with the seismological observations. In such bimaterial systems, it has been demonstrated that intersonic crack propagation is possible even under remote loading conditions (Liu et al. 1993; Lambros and Rosakis 1995a, b, c; Singh and Shukla 1996). The first direct experimental evidence of an intersonic crack growth event was

described by Lambros and Rosakis (1995c). These authors used the optical method of coherent gradient sensing (CGS) and high speed photography to show that under shear dominated loading conditions the interfacial crack tip can exceed the smaller of the two shear wave speeds. They also reported visual experimental evidence of large scale, crack face contact occurring during intersonic crack growth. Liu et al. (1995) obtained the two-dimensional in-plane asymptotic deformation fields surrounding a traction-free crack tip propagating intersonically along an elastic-rigid bimaterial interface which predicted the existence of a shear 'shock wave' discontinuity, that radiates from the crack tip and moves with it the moment that the crack tip speed exceeds the smaller shear wave speed.

Experimental verification of the shear shock wave radiating from the crack tip was provided later by the work of Singh and Shukla (1996) and Singh et al. (1997) by means of high-speed photography and dynamic photoelasticity (unlike CGS, a technique sensitive to shear stresses). These investigators corroborated the existence of a large scale contact of crack faces behind the interfacial crack tip that had been reported by Lambros and Rosakis (1995c). Moreover, they made an additional important observation of a secondary shock front emanating from the trailing edge of the contact zone in addition to the primary shock associated with the moving crack tip. Motivated by the experimental observations, Xu and Needleman (1996) carried out numerical analyses of dynamic interfacial crack growth using a cohesive surface formulation and Huang et al. (1998) carried out an asymptotic analysis of the problem of steady-state interfacial crack growth allowing for large scale, frictional crack face contact. Consistent with experimental observations, the asymptotic analysis accounts for finite contact and predicts the existence of two distinct traveling singular lines of discontinuity, one emanating from the crack tip and the other from the end of the contact zone. For the tensile loading conditions analyzed, Xu and Needleman (1996) found crack speeds only moderately above the Rayleigh wave speed of the more compliant material for an aluminum-PMMA specimen, but in one case, using artificial material properties, a crack speed more than 50% above the lower Rayleigh wave speed was attained. Whenever the lower Rayleigh wave speed was exceeded, the numerical results showed regions of relatively large contact. In the calculation where the lower Rayleigh wave speed was greatly exceeded, there was a single shock wave type disturbance emanating from the crack tip.

In this investigation, fast crack growth along an interface, is simulated using the cohesive surface decohesion formulation in Needleman (1987) and Xu and Needleman (1994) where the failure characteristics are embodied in a phenomenological constitutive relation that describes separation along one or more cohesive surfaces. Within this cohesive surface framework, the continuum is characterized by two constitutive relations; one that relates stress and deformation in the bulk material, the other that relates the traction and displacement jump across a cohesive surface. The parameters characterizing the cohesive surface separation law include a strength and the work of separation per unit area so that a characteristic length enters the formulation. These constitutive relations together with appropriate balance laws and initial and boundary conditions completely

specify the initial-boundary problem. Fracture, when it occurs, emerges as a natural outcome of the loading history. No additional assumptions concerning crack initiation or crack propagation criteria are needed. Crack initiation and the crack speed history are outcomes of the analyses. This framework was used in Xu and Needleman (1995, 1996) to investigate dynamic interfacial crack growth under tensile loading conditions. Here, the configuration in the experiments of Lambros and Rosakis (1995a,b) is modeled where the crack is subject primarily to shear loading. Plane strain conditions are assumed and a single cohesive surface along the interface between the two solids is specified so that the crack is constrained to grow along the bond line. Calculations are carried out for a steel-PMMA bimaterial. The focus is on the effect of loading rate and bond strength on the evolution of the crack speed and on the crack tip stress and deformation fields that develop.

2. Formulation and numerical method

The formulation and numerical solution procedure follow that in Xu and Needleman (1994, 1996). The difference here lies in the specimen geometry and the loading conditions. A finite strain Lagrangian formulation is used, with the initial undeformed configuration taken as reference, so that all field quantities are considered to be functions of convected coordinates, y^i, which serve as particle labels, and time t. The principle of virtual work is written as

$$\int_V \mathbf{s}:\delta\mathbf{F}\,\mathrm{d}V - \int_{S_{\mathrm{int}}} \mathbf{T}\cdot\delta\boldsymbol{\Delta}\,\mathrm{d}S = \int_{S_{\mathrm{ext}}} \mathbf{T}\cdot\delta\mathbf{u}\,\mathrm{d}S - \int_V \rho\frac{\partial^2\mathbf{u}}{\partial t^2}\cdot\delta\mathbf{u}\,\mathrm{d}V, \tag{1}$$

$\mathbf{s}$ is the nonsymmetric nominal stress tensor, $\mathbf{u}$ is the displacement vector, $\mathbf{F}$ is the deformation gradient, $\boldsymbol{\Delta}$ is the displacement jump across the cohesive surface, $\mathbf{A}:\mathbf{B}$ denotes $A^{ij}B_{ji}$, and V, S_{ext} and S_{int} are the volume, external surface area and internal cohesive surface area, respectively, of the body in the reference configuration. The density of the material in the reference configuration is ρ and the traction vector $\mathbf{T}$ and the reference configuration normal $\mathbf{n}$ are related by $\mathbf{T}=\mathbf{n}\cdot\mathbf{s}$. Also, $\mathbf{s}=\mathbf{F}^{-1}\cdot\tau$, where τ is the Kirchhoff stress, $\tau=\det(\mathbf{F})\sigma$, with σ being the Cauchy stress.

Computations are carried out for the edge-cracked bimaterial specimen shown in Fig. 1, which models the experimental configuration used in a series of experiments, e.g. Liu et al. (1993), Lambros and Rosakis (1995c), Singh et al. (1997). In the reference configuration, the specimen has height L, width w and a crack of length a_i along $y^2=0$ (see Fig. 1). Plane strain conditions are assumed to prevail in the analyses although the experiments are carried out for relatively thin specimens. A Cartesian coordinate system is used as reference, with the y^1–y^2 plane as the plane of deformation. The origin of the coordinate system is at the initial crack tip.

At $t = 0$, the body is stress free and at rest. A normal velocity is prescribed on

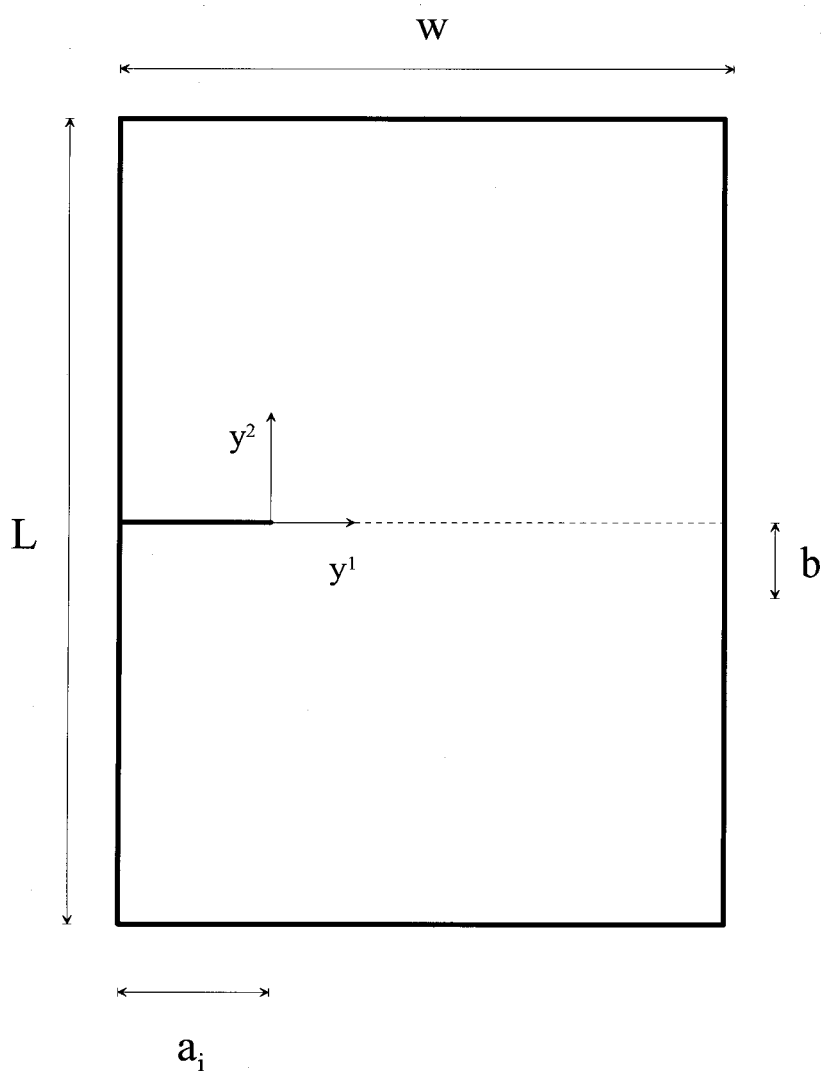

Fig. 1. Geometry of the specimen.

the edge $y^1 = w - a_i$, along the interval $-b \leq y^2 \leq 0$, with the shear traction taken to vanish there. The remaining external surfaces of the specimen are traction free. Hence, the boundary conditions are

$$T^1 = 0, \quad T^2 = 0 \quad \text{on } y^2 = 0 \text{ and } y^1 < 0, \tag{2}$$

$$T^1 = 0, \quad T^2 = 0 \quad \text{on } y^2 = \pm L/2, \quad y^1 = -a_i, \tag{3}$$

$$T^1 = 0, \quad T^2 = 0 \quad \text{on } y^1 = w - a_i \text{ where } y^2 > 0 \text{ or } y^2 < -b, \tag{4}$$

$$u^1 = -\int V(t)\mathrm{d}t, \quad T^2 = 0 \quad \text{on } y^1 = w - a_i \text{ and } -b \le y^2 \le 0, \tag{5}$$

where in (5)

$$V(t) = \begin{cases} V_1 t/t_\mathrm{r}, & \text{for } t \le t_\mathrm{r}; \\ V_1, & \text{for } t > t_\mathrm{r} \end{cases}. \tag{6}$$

The specimen dimensions are given by $L = 30$ cm, $w = 12.5$ cm and $a_i = 2.5$ cm. The length of the boundary over which impact occurs is specified by $b = 5$ cm, the rise time is fixed at 0.1 μs and the impact velocity is varied.

The continuum is characterized by two constitutive relations; a volumetric constitutive law that relates stress and strain, and a cohesive surface constitutive relation between the tractions and displacement jumps across a single cohesive surface that lies along the line $y^2 = 0$ in front of the initial crack.

The volumetric constitutive law for each material is taken to be that for an isotropic hyperelastic solid so that

$$\mathbf{S} = \frac{\partial W}{\partial \mathbf{E}}, \quad W = \frac{1}{2}\mathbf{E}:\mathbf{L}:\mathbf{E}. \tag{7}$$

Here W is the strain energy density and $\mathbf{L}$ is the tensor of isotropic elastic moduli with two elastic constants, Young's modulus E and Poisson's ratio ν. The second Piola–Kirchhoff stress, $\mathbf{S}$, and the Lagrangian strain, $\mathbf{E}$, are given by

$$\mathbf{S} = \mathbf{s} \cdot \mathbf{F}^{-\mathrm{T}}, \quad \mathbf{E} = \frac{1}{2}(\mathbf{F}^T \cdot \mathbf{F} - \mathbf{I}), \tag{8}$$

where $\mathbf{I}$ is the identity tensor, $(\,)^{-1}$ denotes the inverse, and $(\,)^{\mathrm{T}}$ denotes the transpose.

The constitutive law for the cohesive surface is taken to be elastic with the traction given by

$$\mathbf{T} = -\frac{\partial \phi}{\partial \mathbf{\Delta}}. \tag{9}$$

The specific form of the potential ϕ used in this investigation is that given in Xu and Needleman (1993), which allows for tangential, as well as normal, decohesion

$$\begin{aligned} \phi(\mathbf{\Delta}) = \phi_\mathrm{n} + \phi_\mathrm{n} \exp\left(-\frac{\Delta_\mathrm{n}}{\delta_\mathrm{n}}\right) \Bigg\{ \left[1 - r + \frac{\Delta_\mathrm{n}}{\delta_\mathrm{n}}\right] \frac{1-q}{r-1} \\ - \left[q + \left(\frac{r-q}{r-1}\right)\frac{\Delta_\mathrm{n}}{\delta_\mathrm{n}}\right] \exp\left(-\frac{\Delta_t^2}{\delta_t^2}\right) \Bigg\}, \end{aligned} \tag{10}$$

where $\Delta_n = \mathbf{n}\cdot\boldsymbol{\Delta}$ and $\Delta_t = \mathbf{t}\cdot\boldsymbol{\Delta}$, with $\mathbf{n}$ and $\mathbf{t}$ as the normal and tangent, respectively, to the surface at a given point in the reference configuration. Also, $q=\phi_t/\phi_n$ and $r=\Delta_n^*/\delta_n$, where Δ_n^* is the value of Δ_n after complete shear separation with normal traction $T_n=0$. The normal work of separation, ϕ_n, and the shear work of separation, ϕ_t, can be written as

$$\phi_n = e\,\sigma_{max}\,\delta_n \quad \phi_t = \sqrt{\frac{e}{2}}\tau_{max}\,\delta_t. \tag{11}$$

Here, $e=\exp(1)$, σ_{max} and τ_{max} are the cohesive surface normal strength and tangential strength, respectively, and δ_n and δ_t are corresponding characteristic lengths.

The normal traction across the surface, T_n, as a function of Δ_n with $\Delta_t \equiv 0$ is shown in Fig. 2(a). The maximum value of $-T_n$ is σ_{max} and occurs when $\Delta_n=\delta_n$. The variation of shear traction T_t with Δ_t when $\Delta_n \equiv 0$ is shown in Fig. 2(b). The maximum value of $|T_t|=\tau_{max}$ is attained when $|\Delta_t| = \sqrt{2}\delta_t/2$.

The finite element discretization is based on linear displacement triangular elements that are arranged in a 'crossed-triangle' quadrilateral pattern. The mesh used in the calculations, shown in Fig. 3, has 61,312 quadrilateral elements and 247,424 degrees of freedom. There is a uniform region in front of the initial crack of 8×400 rectangular quadrilateral elements, with each rectangle being 75×100 μm, and the mesh spacing is gradually increased in size out to the boundary. The equations that result from substituting the finite element discretization into (1) are of the form

$$\mathbf{M}\frac{\partial^2\mathbf{U}}{\partial t^2} = \mathbf{R}, \tag{12}$$

where $\mathbf{M}$ is a mass matrix, $\mathbf{U}$ is the nodal displacement vector and $\mathbf{R}$ is the nodal force vector. The equations of motion (12) are integrated numerically by an explicit integration procedure, the Newmark β-method with $\beta=0$, Belytschko et al. (1976). A lumped mass matrix is used instead of the consistent mass matrix, since this has been found preferable for explicit time integration procedures, from the point of view of accuracy as well as computational efficiency, Krieg and Key (1973).

3. Numerical results

The calculations are carried out for a steel-PMMA specimen, with the loading applied on the steel side ($y^2 < 0$) of the bimaterial specimen. The PMMA material properties are specified by $E = 3.24$ GPa, $\nu=0.35$ and $\rho=1190$ kg/m^3. The corresponding values for steel are $E = 208$ GPa, $\nu=0.3$ and $\rho=7830$ kg/m^3. In PMMA, the speeds of dilational, shear and Rayleigh waves are $c_d=2090$ m/s, $c_s=1004$ m/s, $c_R=938$ m/s, respectively, while in steel $c_d=5980$ m/s, $c_s=3196$ m/s and $c_R=2960$ m/s.

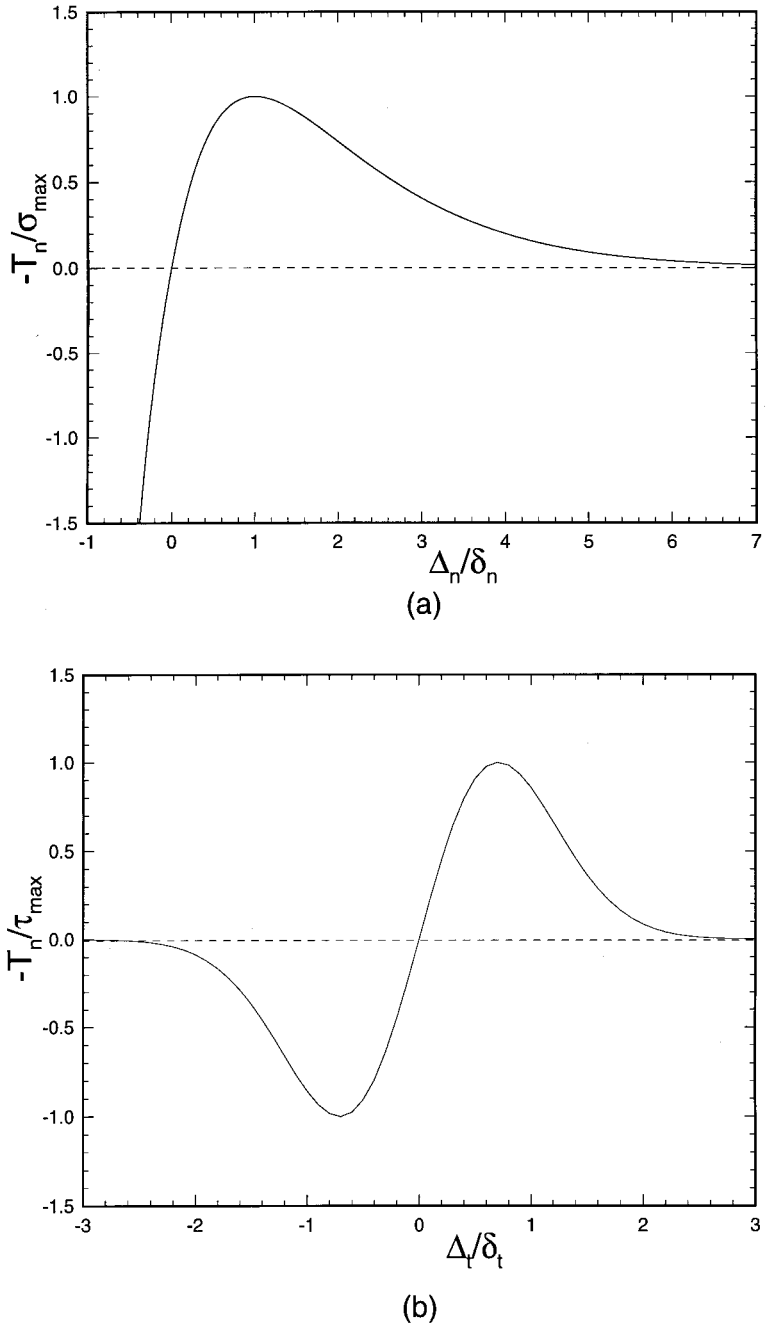

Fig. 2. (a) Normal traction, T_n, across the cohesive surface as a function of Δ_n with $\Delta_t \equiv 0$. (b) Shear traction, T_t, across the cohesive surface as a function of Δ_t for $\Delta_n \equiv 0$.

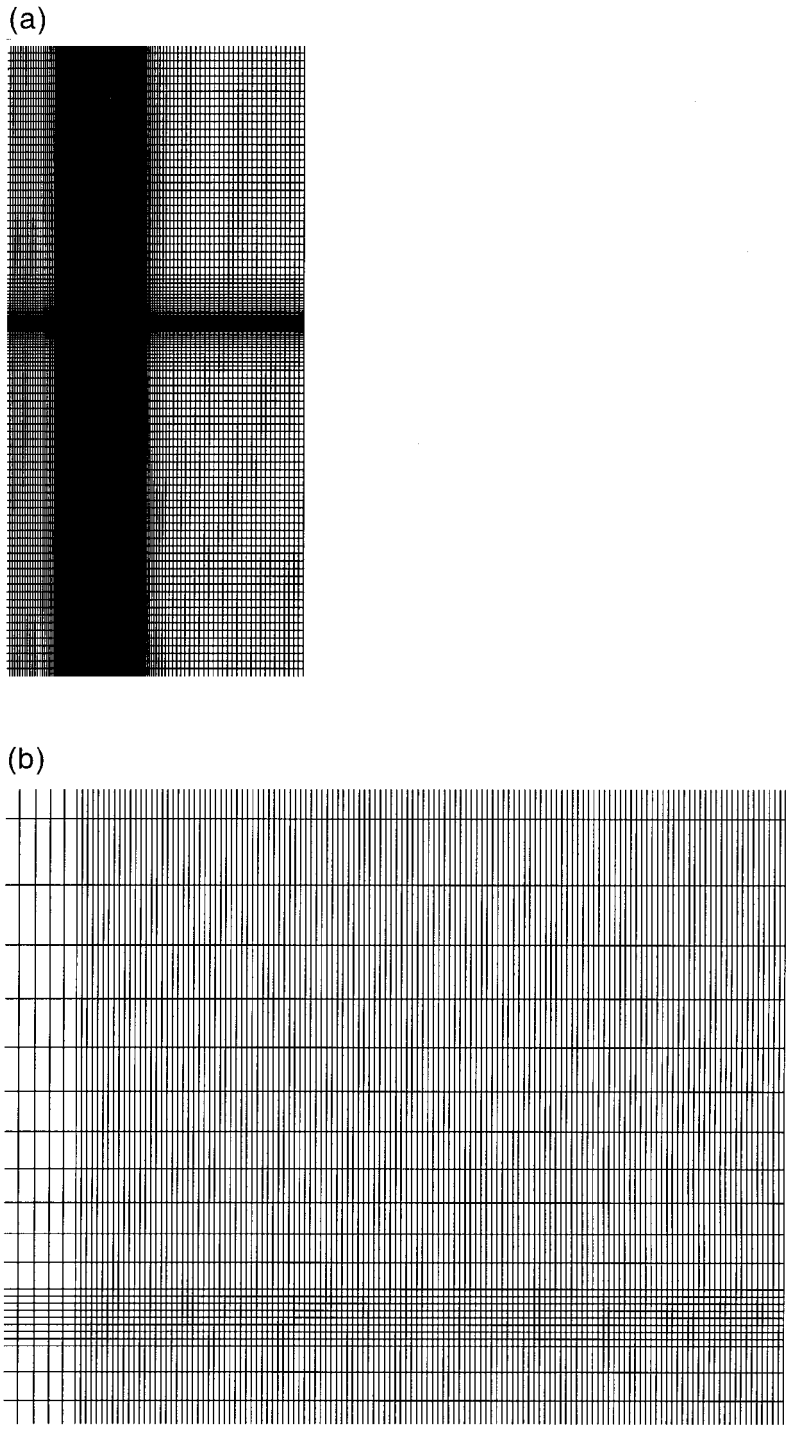

Fig. 3. (a) The full specimen. (b) The mesh near the initial crack tip. The uniform mesh ahead of the initial crack consists of 400× 8 rectangles of dimension 75 × 100 μm.

The main effect of the impact loading is a wave carrying a compressive stress S^{11} that propagates across the specimen and reaches the crack tip at 16.7 μs. Fig. 4 shows the stress distribution in the specimen at $t = 16$ μs for a case with $V_1 = 20$ m/s. At 20.9 μs, the loading wave reaches the free surface at $y^1 = -a_i$ and at 25.1 μs the reflected wave reaches the initial crack tip. A time shortly after this is shown in Fig. 5, where $t = 29$ μs. The large compressive stress parallel to the crack line under the impact region is seen in Fig. 5(a). The overall stress pattern is fairly complex due to the elastic mismatch across the bond line and due to reflections from the free surfaces. A general feature is that the largest stress magnitudes occur in the steel away from the bond line. At 41.8 μs, the reflected wave reaches the impact surface. The time in Fig. 6, where $t = 38$ μs, is somewhat before this and the largest stress magnitude in the vicinity of the bond line remains the compressive S^{11} stress although the details of the stress distributions have changed due to wave effects. In Figs. 4–6, the magnitudes of all stress components remain small in the PMMA ($y^2 > 0$) and the largest stress magnitudes in the steel ($y^2 < 0$) occur at the corner of the impact region on the free surface. Large positive values of the opening stress S^{22} are not seen near the

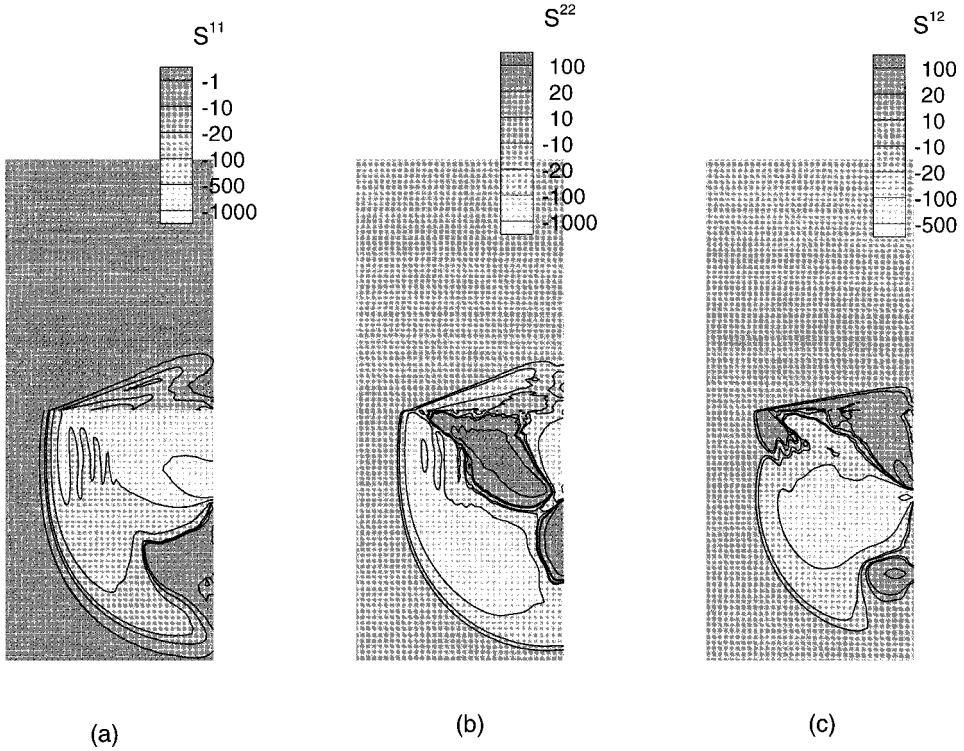

Fig. 4. Contours of stress components for $V_1 = 20$ m/s and $\sigma_{max} = \sigma^{PMMA}/2$ at $t = 16$ μs. (a) S^{11}. (b) S^{22}. (c) S^{12}.

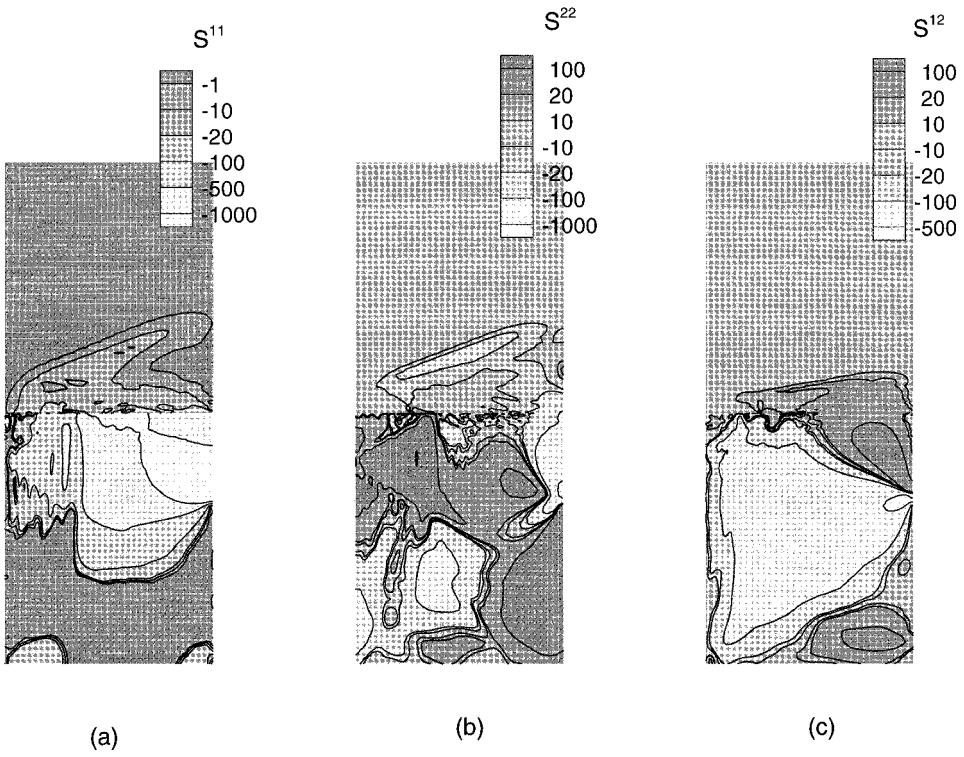

Fig. 5. Contours of stress components for $V_1 = 20$ m/s and $\sigma_{max} = 3\sigma^{PMMA}/4$ at $t = 29$ μs. (a) S^{11}. (b) S^{22}. (c) S^{12}.

bond line. In fact, the S^{22} stress contour due to the propagating crack that is evident in Fig. 6(b) corresponds to a negative (compressive) value.

First a parametric study is reported on the effects of impact velocity and bond strength on the crack growth history. Then the numerical predictions are compared with experimental observations.

3.1. Parameter study

The interface is characterized by $\delta_n = 0.4$ μm, $\delta_t = 0.931$ μm, $q = 1$ and $r = 0$. Also, in all cases, $\sigma_{max} = \tau_{max}$. The ratio δ_t/δ_n is set by the condition $q = 1$ with $\sigma_{max} = \tau_{max}$. With $\sigma_{max} = E^{PMMA}/10 = 324$ MPa, $\phi_n = \phi_t = 352.3$ J/m^2.

The impact velocity V_1 and the bond strength σ_{max} are varied, with values of V_1 ranging from 2 to 30 m/s and values of $\sigma_{max} = \tau_{max}$ of $\sigma^{PMMA}/20$ (16.2 MPa), $\sigma^{PMMA}/4$ (81 MPa), $\sigma^{PMMA}/2$ (162 MPa) and $3\,\sigma^{PMMA}/4$ (243 MPa), where $\sigma^{PMMA} = E^{PMMA}/10$.

Fig. 7 shows curves of crack speed vs time for various impact velocities for a bond strength of $3\,\sigma^{PMMA}/4$, Fig. 7(a), and for a bond strength of $\sigma^{PMMA}/2$, Fig.

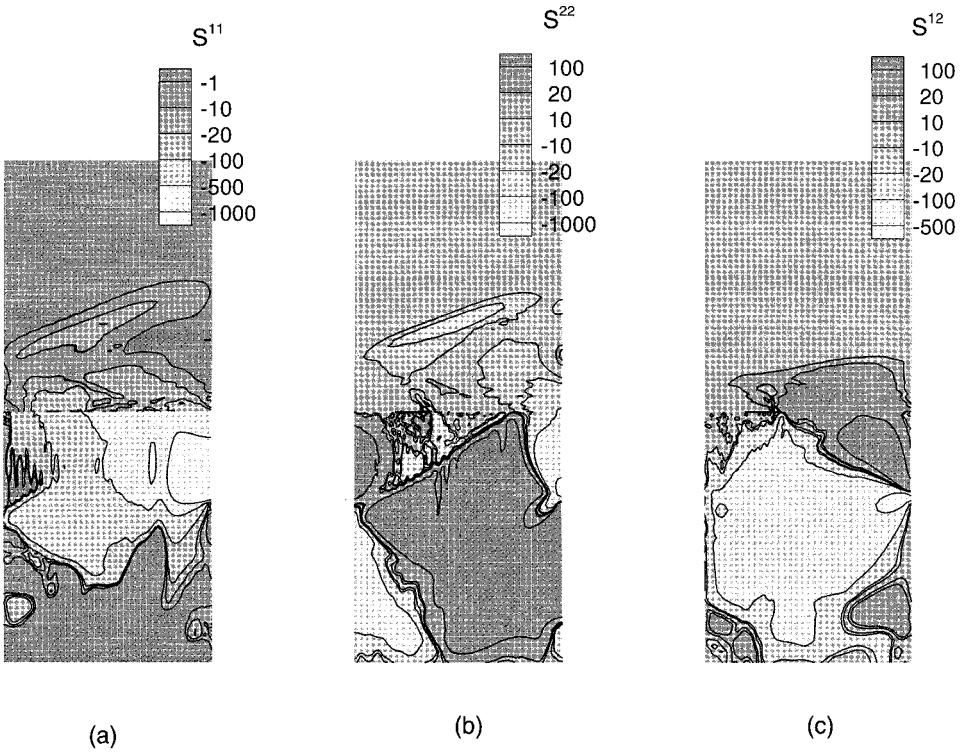

Fig. 6. Contours of stress components for $V_1 = 20$ m/s and $\sigma_{max} = 3\sigma^{PMMA}/4$ at $t = 38$ μs. (a) S^{11}. (b) S^{22}. (c) S^{12}.

7(b). The first step in computing the crack speed is to record the crack location. This is defined in one of two ways: (i) the time at which, for a given node along the cohesive surface, Δ_n first becomes greater than or equal to $5\delta_n$; or (ii) the time at which, for a given node along the cohesive surface, Δ_t first becomes greater than or equal to $5\delta_t$. The crack location based on Δ_n is referred to as the opening crack location, while the crack location based on Δ_t is referred to as the shear crack location. The crack speed vs time curves are then computed from this data by successive three point least squares linear fits; i.e. through points 1–3, points 2–4, etc. As can be seen in Fig. 7, the initiation of crack growth varies with the impact speed. Unless specifically stated otherwise, crack speeds are computed using Δ_t and hence are the shear crack speeds.

The most striking feature of the crack growth vs time curves in Fig. 7 is the abrupt transition between two types of crack growth history. For a sufficiently low impact velocity, the crack speed approaches the Rayleigh wave speed of PMMA (938 m/s), while if the impact velocity is above a transition value the mean crack speed increases to about 1800 m/s. The transition impact velocity in Fig. 7(a) is between 19.75 m/s and 20 m/s. With $V_1 = 19.75$ m/s crack growth

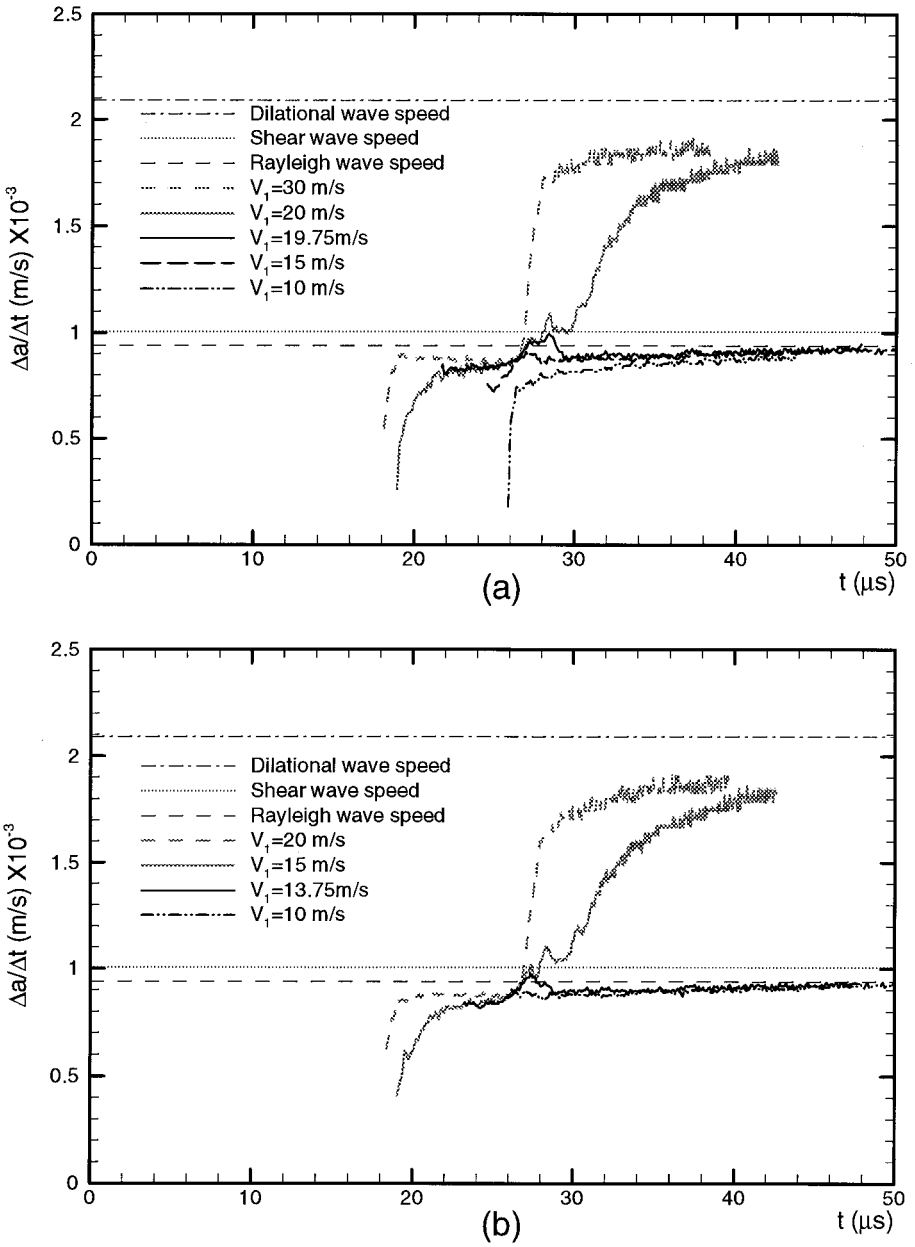

Fig. 7. Curves of crack speed, $\Delta a/\Delta t$ vs time, t, for various values of the impact velocity, V_1. (a) With the cohesive strength of the bond line equal to $3\,\sigma^{\mathrm{PMMA}}/4$. (b) With the cohesive strength of the bond line equal to $\sigma^{\mathrm{PMMA}}/2$.

begins at 21.6 μs. The crack speed increases to 995 m/s at $t = 28.4$ μs, falls to 885 m/s and then slowly increases to about 938 m/s (the Rayleigh speed of PMMA) as the end of the uniform mesh region is approached. When the impact velocity is increased to 20 m/s, crack growth begins slightly earlier and follows essentially the same trajectory as with an impact velocity of 19.75 m/s until $t = 28.4$ μs. The crack speed then continues to increase to a local maximum of 1059 m/s at 28.7 μs, and then decreases to 995 m/s at $t = 29.5$ μs. After this local minimum, the crack speed increases to ≈ 1800 m/s. For values of the impact velocity below 19.75 m/s, the onset of crack growth is delayed, to 26.4 μs for $V_1 = 10$ m/s, and the crack speed increases gradually to the PMMA Rayleigh wave speed. Increasing the impact velocity to 30 m/s gives rise to earlier crack growth and a steeper rise to a crack speed that is very close to the one reached with $V_1 = 20$ m/s. In Fig. 7(b), a similar transition is seen where the transition impact velocity is between 12.5 and 15 m/s.

Crack speed vs time curves for bond strength values of $\sigma^{\mathrm{PMMA}}/4$ and $\sigma^{\mathrm{PMMA}}/20$ are shown in Fig. 8. The same two sorts of crack speed histories are seen, but with lower transition impact velocities. In Fig. 8(a), where the bond strength is $\sigma^{\mathrm{PMMA}}/4$ the transition impact velocity is between 8.75 and 10 m/s, while the transition impact velocity is between 2 and 3 m/s with a bond strength of $\sigma^{\mathrm{PMMA}}/20$, Fig. 8(b). The very high crack speed seen in Fig. 8(b) at $t = 27.6$ μs is a consequence of the crack extending over two mesh spacings in a very short time interval (recall that the crack location is defined by Δ_t exceeding 5 δ_t). One possible explanation for this is that the jump in crack speed is associated with slip initiating ahead of the main crack, although the mesh used here is too coarse to resolve that. In Figs. 7 and 8, Δ_n is used to identify the crack location for some cases where the crack speed remains less than the PMMA Rayleigh wave speed. As will be shown subsequently (Fig. 11(a)), the computed crack speed in such circumstances is insensitive to whether Δ_t or Δ_n is used to define the crack location.

The dependence of the transition impact velocity, v_{trans}, on the cohesive strength of the bond line is shown in Fig. 9. The squares mark the smallest impact velocity for which the crack speed exceeds the PMMA Rayleigh wave speed, while the circles mark the highest impact velocity for which the crack speed remained less than the PMMA Rayleigh wave speed. For $\sigma_{\max}/\sigma^{\mathrm{PMMA}} = 3/4$, calculations were carried out to narrow down the transition impact velocity to between 19.75 and 20 m/s. For the other values of $\sigma_{\max}/\sigma^{\mathrm{PMMA}}$ the transition was bracketed by values of the impact velocity differing by 1–1.25 m/s. For bond strength values between $\sigma^{\mathrm{PMMA}}/4$ and $3\,\sigma^{\mathrm{PMMA}}/4$, there is a linear fit to the square points in Fig. 9. However, the transition impact velocity for the weakest bond strength falls well below the linear extrapolation of that fit.

The crack speed vs time curves for $V_1 = 5$ m/s, $\sigma_{\max}/\sigma^{\mathrm{PMMA}} = 1/20$, $V_1 = 10$ m/s, $\sigma_{\max}/\sigma^{\mathrm{PMMA}} = 1/4$, $V_1 = 20$ m/s, $\sigma_{\max}/\sigma^{\mathrm{PMMA}} = 1/2$, $V_1 = 20$ m/s, $\sigma_{\max}/\sigma^{\mathrm{PMMA}} = 3/4$ and $V_1 = 30$ m/s, $\sigma_{\max}/\sigma^{\mathrm{PMMA}} = 3/4$ are plotted in Fig. 10. The limiting crack speed of ≈ 1800 m/s (which is about 10% lower than the PMMA dilational wave speed) depends only weakly, if at all, on the impact velocity and bond strength. In

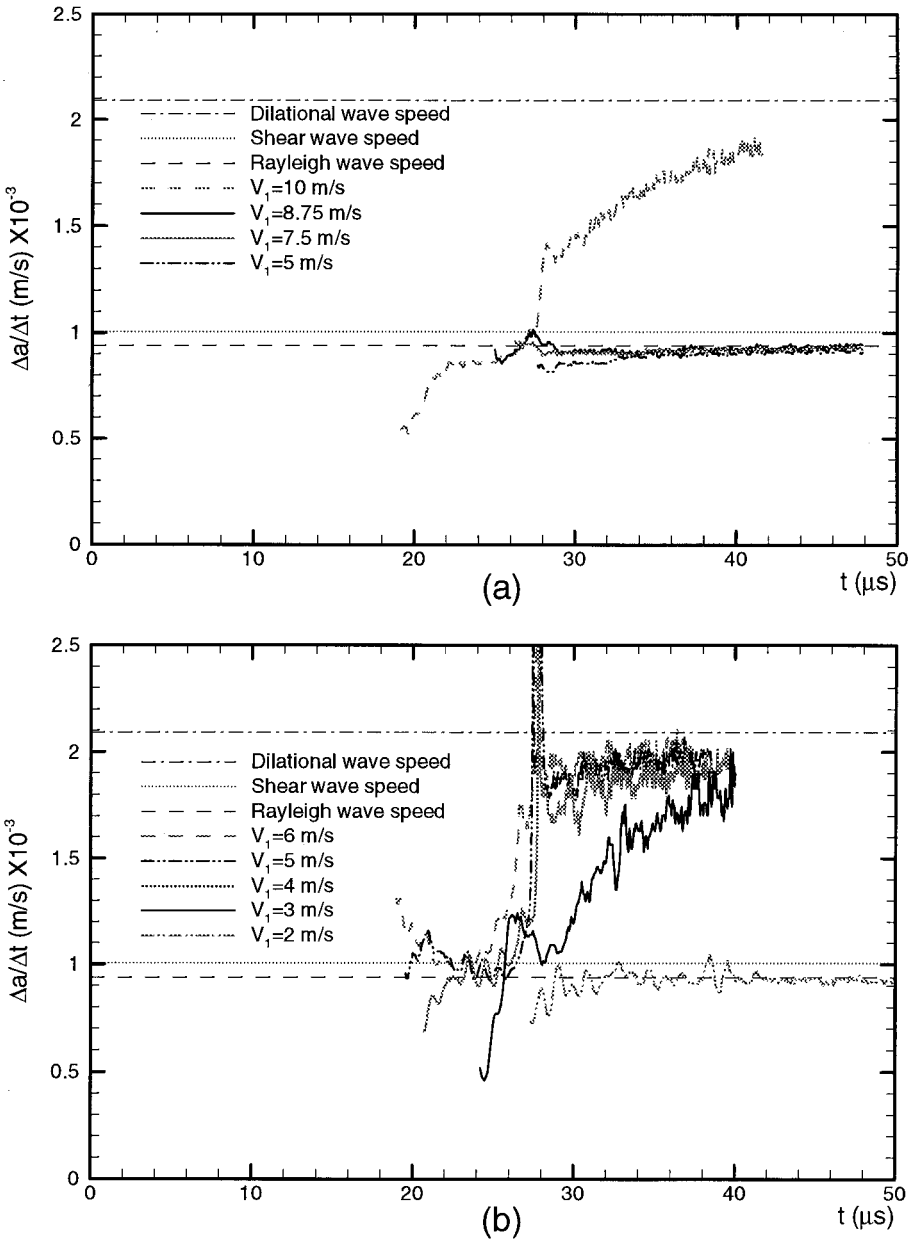

Fig. 8. Curves of crack speed, $\Delta a/\Delta t$ vs time, t, for various values of the impact velocity, V_1. (a) With the cohesive strength of the bond line equal to $\sigma^{\mathrm{PMMA}}/4$. (b) With the cohesive strength of the bond line equal to $\sigma^{\mathrm{PMMA}}/20$.

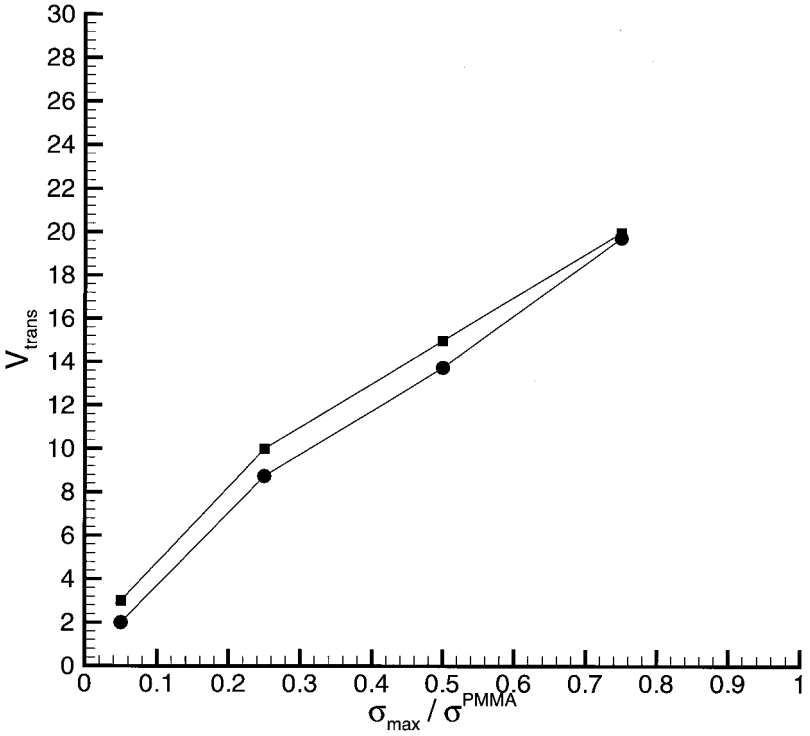

Fig. 9. The dependence of the transition impact velocity, V_{trans}, on the cohesive strength of the bond line, σ_{max}.

all cases, the crack speed first exceeds the PMMA Rayleigh wave speed at a bit after 25 μs, which is when the reflected wave reaches the crack tip. The small differences in times seen in Fig. 10 are most likely a consequence of differences in the amount of crack growth that occurs with the first loading wave.

Fig. 11 shows a comparison of crack speeds computed using Δ_t and Δ_n to define the crack location. In Fig. 11(a), the bond strength is $3\,\sigma^{PMMA}/4$ and results for $V_l = 10$ m/s and $V_l = 20$ m/s are shown. With $V_l = 10$ m/s, except for initiation, the crack speed is insensitive to whether Δ_t or Δ_n is used to define the crack location. For both $V_l = 10$ m/s and for $V_l = 20$ m/s, using Δ_n to define the crack location leads to a somewhat later time for crack initiation than when the crack location is based on the value of Δ_t. In addition, with Δ_n defining the crack location, the crack speed is high initially and then decreases. This is most likely due to the rather coarse mesh (relative to δ_n) and these high initial values were not shown in Figs. 7 and 8. On the other hand, when the crack location is defined using Δ_t, the crack speed increases smoothly, but rapidly, in the early stages of crack growth. This behavior is consistent with experimentally recorded crack speeds where the crack tip location was defined as the first visible singularity across the bond line, i.e. the point of convergence of dense CGS or photoelastic

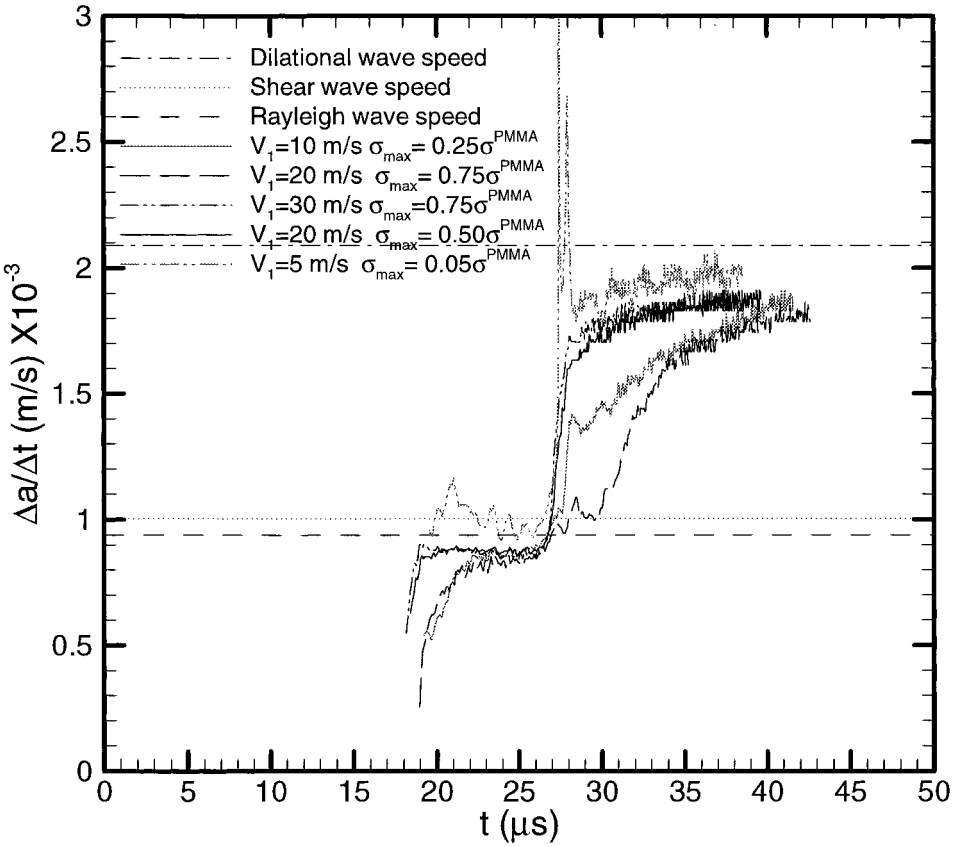

Fig. 10. Comparison of the crack speed, $\Delta a/\Delta t$ vs time, t, curves for $V_1 = 10$ m/s, $\sigma_{max}/\sigma^{PMMA} = 1/4$, $V_1 = 20$ m/s, $\sigma_{max}/\sigma^{PMMA} = 1/2$, $V_1 = 30$ m/s, $\sigma_{max}/\sigma^{PMMA} = 3/4$, $V_1 = 20$ m/s, $\sigma_{max}/\sigma^{PMMA} = 3/4$ and $V_1 = 5$ m/s, $\sigma_{max}/\sigma^{PMMA} = 1/20$.

fringes, see e.g. Lambros and Rosakis (1995c). With $V_1 = 20$ m/s, the crack speeds computed from the two definitions of crack location are in very good agreement until $\Delta a/\Delta t \approx 1600$ m/s when the crack speed based on the normal opening, Δ_n, begins to oscillate. As will be shown subsequently, these oscillations are associated with the occurrence of discrete crack face contact regions separated by micro-crack like openings behind the main shear crack tip. The oscillations are essentially due to the transient nature of the contact phenomenon. The crack speed based on the tangential or shear displacement jump, Δ_t, is close to the mean of the oscillating speed obtained when Δ_n is used to define the crack location. In Fig. 11(b), where the bond strength is $\sigma^{PMMA}/20$ and the impact velocity is 5 m/s, when the crack location is defined by the normal displacement jump Δ_n, crack growth begins later than when the crack location is defined by the tangential displacement jump Δ_t and the mean crack speed based on Δ_n is significantly less

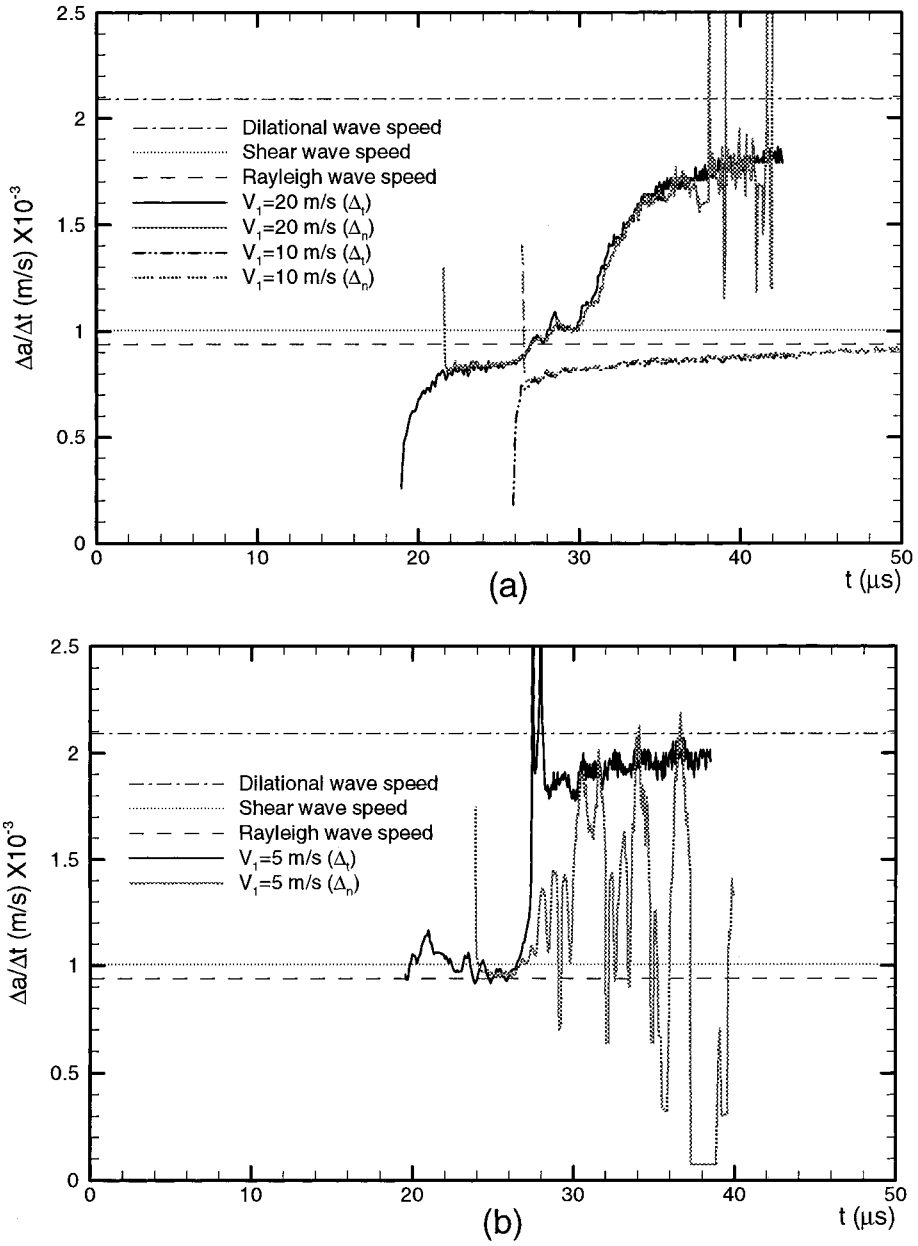

Fig. 11. Curves of crack speed, $\Delta a/\Delta t$ vs time, t, showing the effect of using the normal displacement jump, Δ_n, or the tangential displacement jump, Δ_t, to define the crack location. (a) $\sigma_{max}/\sigma^{PMMA} = 3/4$. (b) $\sigma_{max}/\sigma^{PMMA} = 1/20$.

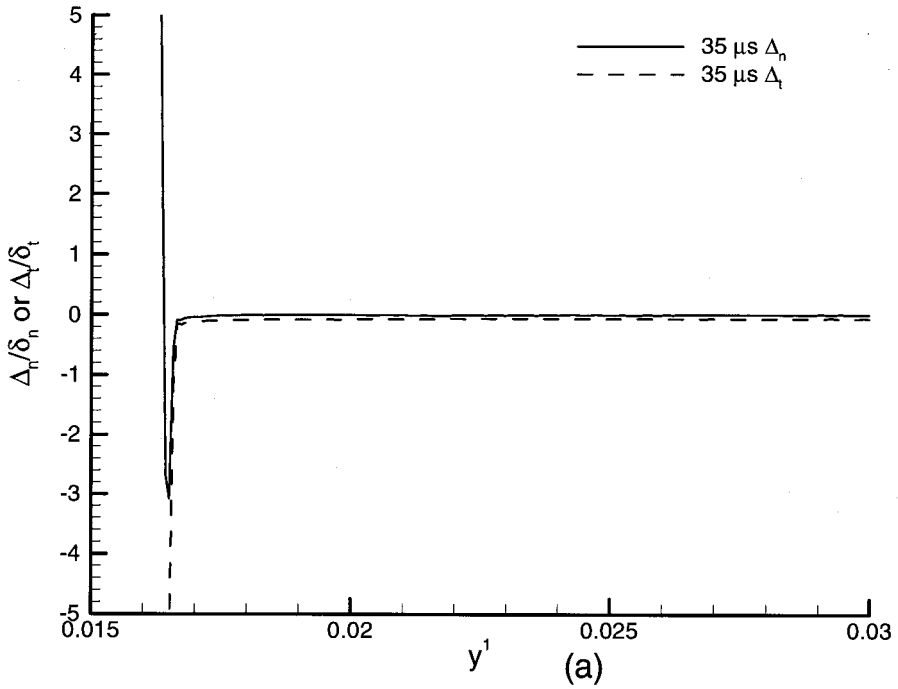

Fig. 12. (a) Δ_n and Δ_t for $V_1 = 20$ m/s at $t = 35$ μs. (b) Comparison of the normal displacement jump across the bond line, Δ_n, for $V_1 = 10$ m/s and $V_1 = 20$ m/s at $t = 39.75$ μs. (c) Comparison of the tangential displacement jump across the bond line, Δ_t, for $V_1 = 10$ m/s and $V_1 = 20$ m/s at $t = 39.75$ μs. In all cases, $\sigma_{max} = 3\ \sigma^{PMMA}/4$ and Δ_n is normalized by the cohesive characteristic length δ_n while Δ_t is normalized by the cohesive characteristic length δ_t. In (b) and (c), the upper axis pertains to the calculation with $V_1 = 20$ m/s and the lower axis to the calculation with $V_1 = 10$ m/s. Distances are in meters.

than the crack speed based on Δ_t. This indicates that the 'opening crack' trails the 'shear crack'. Presumably, this is also the case for the higher strength bond, but the difference in speeds is too small to be evident.

A comparison of the opening, Δ_n, and shear, Δ_t, displacement jumps is shown in Fig. 12 for cases with $\sigma_{max} = 3\ \sigma^{PMMA}/4$. Fig. 12(a) shows curves of Δ_n and Δ_t vs position along the bond line for $V_1 = 20$ m/s at $t = 35$ μs on the same plot. The shear crack tip is in front of the contact zone. Two crack tip profiles at $t = 39.75$ μs are compared in Fig. 12(b) and (c). Fig. 12(b) shows the normal opening, Δ_n, and (c) the tangential opening, Δ_t. One curve is for $V_1 = 10$ m/s, while the other is for $V_1 = 20$ m/s. With $V_1 = 10$ m/s, the crack speed is 875 m/s and both the opening and shear displacement jumps give rise to a crack profile that is monotonically opening. On the other hand, with $V_1 = 20$ m/s the current crack speed is 1790 m/s and the opening has an oscillating profile, with two regions of positive opening displacement ahead of the main crack. These correspond to finite

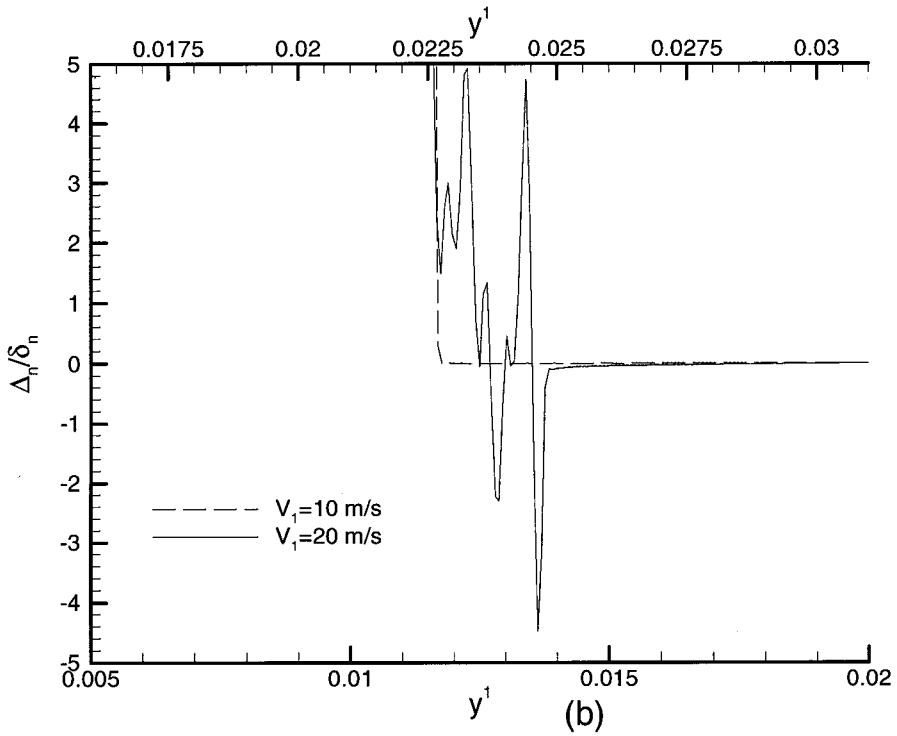

Fig. 12 (*continued*)

size openings separating regions of crack face contact, which are referred to as micro-cracks. These micro-cracks are 350 and 230 μm in size and the initiation of a third micro-crack can be seen. Comparing Fig. 12(b) and (c) shows that when the crack speed is below the PMMA Rayleigh wave speed the location of the crack tip is the same whether it is defined in terms of Δ_n or Δ_t, but that when crack speed exceeds the PMMA Rayleigh wave speed, the crack location based on Δ_t is in front of the micro-cracks; in fact at $t = 39.75$ μs with $V_1 = 20$ m/s, the shear crack tip is at the front of the leading contact zone as it is at $t = 35$ μs in Fig. 12(a). The general picture is that for crack speeds less than the PMMA Rayleigh wave speed, the opening and shear crack positions coincide. When the crack speed increases beyond the PMMA Rayleigh wave speed, the shear crack tip moves ahead of the opening crack tip. When micro-cracks form, the shear crack tip is in front of the micro-cracks, while the tip of the main opening crack is behind the micro-cracks.

Fig. 13 shows the normal displacement jump across the bond line near the crack tip at various times for the calculation having $V_1 = 20$ m/s and $\sigma_{max}/\sigma^{PMMA} = 3/4$. At $t = 29$ μs, in Fig. 13(a), the crack speed is 1029 m/s, 10% above the PMMA Rayleigh wave speed. A slightly compressive displacement jump,

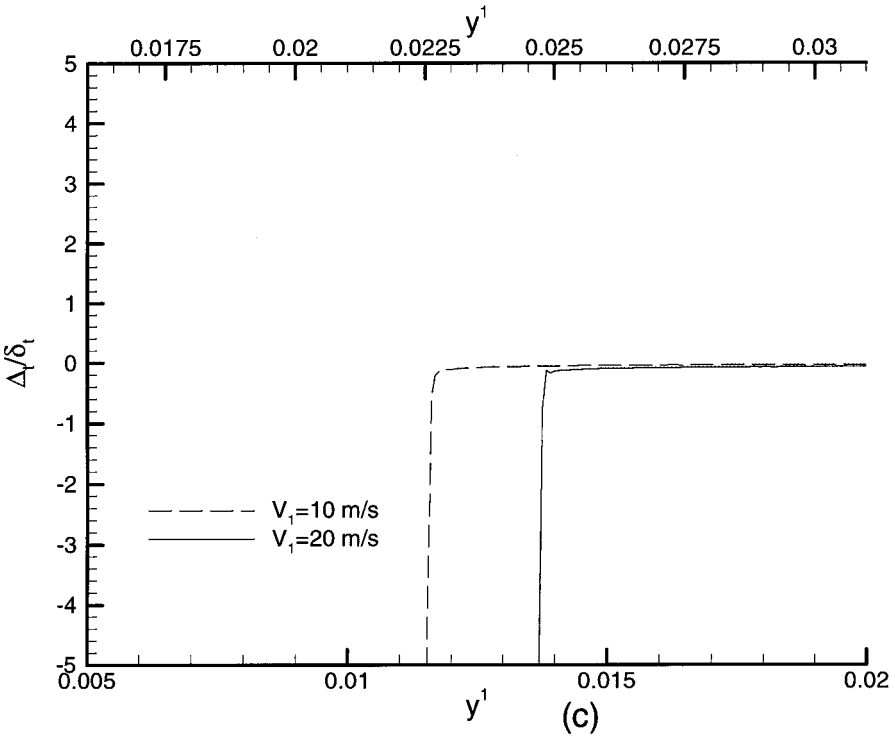

Fig. 12 (*continued*)

negative Δ_n, is evident just in front of the opening crack tip. The maximum magnitude of this compressive displacement jump increases from 0.1 δ_n to 2.6 δ_n between 31 and 33 μs, while the crack speed increases from 1144 m/s to 1500 m/s. Thereafter, both the mean crack speed and the peak magnitude of the compressive displacement jump increase much more slowly. As seen in Fig. 13(b), after t = 35 μs, Δ_n begins to oscillate behind the current crack tip. The amplitude of the oscillation grows and the mean value shifts downward so that by t = 38 μs, the result is two small micro-cracks ahead of the main opening crack tip. The smaller micro-crack is 200 μm in length and the larger is about 300 μm long. The algorithm for identifying the crack location does not distinguish between the main crack and one of the micro-cracks, which accounts for the very large oscillations in crack speed seen when the crack location is based on Δ_n. Each of the oscillations at the later times consists of about 3 grid spacings so that these oscillations are not fully resolved with the mesh used. Also, any effect of friction during contact is neglected in the present calculations.

The loading wave induces the development of a negative Δ_n on the free surface of the initial crack. This is attained at $y^1 = -0.01$ m which is much further away from the crack tip than the region shown in Fig. 13. However, it is worth noting that with $V_1 = 20$ m/s, the maximum magnitude is $\Delta_n/\delta_n = -97$ at around 25 μs. At

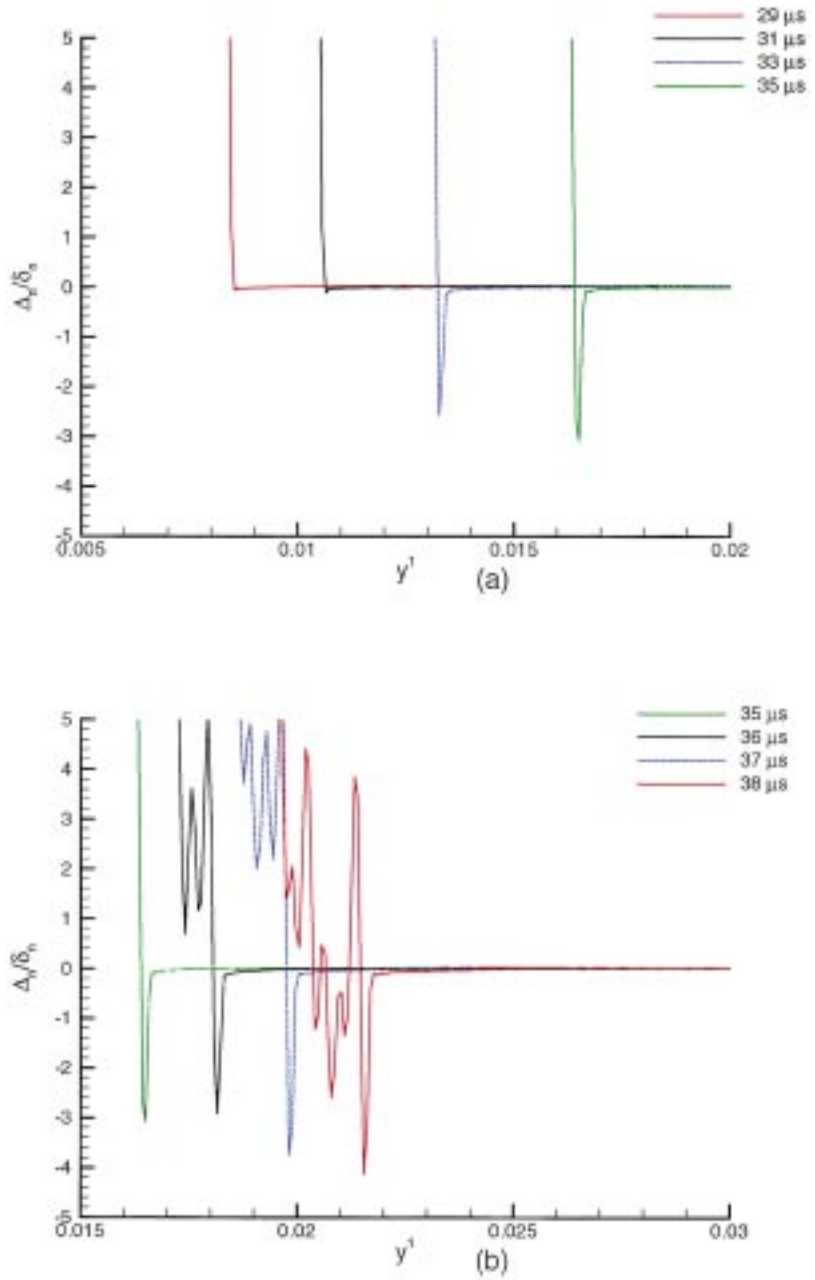

Fig. 13. Evolution of the normal component of the displacement jump across the bond line, Δ_n, for $V_1 = 20$ m/s and $\sigma_{max} = 3\,\sigma^{PMMA}/4$. (a) From 29 to 35 μs. (b) From 35 to 38 μs.

t = 29 μs, the maximum $\Delta_n/\delta_n = -69$, which with $\delta_n = 0.4$ μm corresponds to $\Delta_n = -28$ μm. Subsequently, Δ_n increases along the free surface and is positive all along the initial crack for $t > 32$ μs. For very sharp initial cracks and/or for high values of impact velocity, there is the possibility of contact occurring across the initial crack faces. Such contact, which is not accounted for in the present calculations, could affect the subsequent course of crack growth.

Fig. 14 shows shear crack growth results for two meshes. In the reference mesh, used in the calculations presented here, the grid spacing along the bond line in the uniform mesh region is 75 μm. This mesh is labelled h_0 in Fig. 14. In the other mesh, labelled $h_0/2$, this grid spacing is halved to 37.5 μm. In Fig. 14(a) where the bond strength is $3\,\sigma^{\mathrm{PMMA}}/4$ and the impact velocity is 30 m/s, the two curves are in very good agreement while the crack speed is below the PMMA Rayleigh wave speed. The rapid increase in crack speed occurs about 1.1 μs later and more abruptly for the finer mesh. Once, the crack speed jump has occurred, the mean crack speed for the finer mesh calculation is about 6% less than that for the calculation using the reference h_0 mesh. In Fig. 14(b), the bond strength is $\sigma^{\mathrm{PMMA}}/20$ and the impact velocity is 5 m/s. Here, the crack speed vs time curves are virtually identical except for the increased oscillation amplitude with the $h_0/2$ mesh. Gradients near the crack tip essentially scale with $E/\sigma_{\max}$ times the cohesive characteristic length, see e.g. Morrisey and Rice (1998), so that for a given mesh spacing more accurate results are expected for the lower strength bond calculations.

Contours of S^{22} in the vicinity of the current crack tip at t = 40 μs for $V_1 = 10$ m/s and $\sigma_{\max}/\sigma^{\mathrm{PMMA}} = 3/4$ are shown in Fig. 15. The crack tip is at $y^1 = 0.012$ m. Two regions of stress concentration can be seen emanating from the crack tip into the PMMA; a region of positive S^{22} ahead of the shear crack tip and a region of negative S^{22} behind the shear crack tip.

Fig. 16 shows contours of S^{22} at various stages of crack growth for the calculation with $V_1 = 20$ m/s and $\sigma_{\max}/\sigma^{\mathrm{PMMA}} = 3/4$. In Fig. 16(a), t = 29 μs, Δa = 8.5 mm and $\Delta a/\Delta t$ = 1009 m/s. The values of Δa given here and in the figure captions are based on using Δ_t to identify the crack location. The concentration above the bond line, associated with the crack tip is compressive ($S^{22} < 0$), which, of course, is the opposite sign of the S^{22} stress concentration associated with a mode I crack. There is a tensile region about 0.006 m in front of the crack. At t = 35 μs, Fig. 16(b), where the crack speed is $\Delta a/\Delta t =$ 1624 m/s and the crack has grown to Δa = 0.016 m (since the crack is initially at $y^1 = 0$, Δa corresponds to the value of the y^1-coordinate specifying the crack tip location), the extent of the compressive S^{22} concentration surrounding the crack tip has increased. The intersection of the compressive S^{22} region with the bond line is at the location where the negative Δ_n occurs in Fig. 13 for t = 35 μs. A small secondary compressive S^{22} concentration behind the current crack tip can also be seen. The inclination of the stress contours near the crack tip is consistent with the high crack speed. In Fig. 16(c), where t = 38 μs and $\Delta a/\Delta t$ = 1716 m/s, the region enclosed by the leading −25 MPa contour has grown, but the smaller region enclosed by the −25 MPa contour at about $y^1 = 0.013$ m is about the same

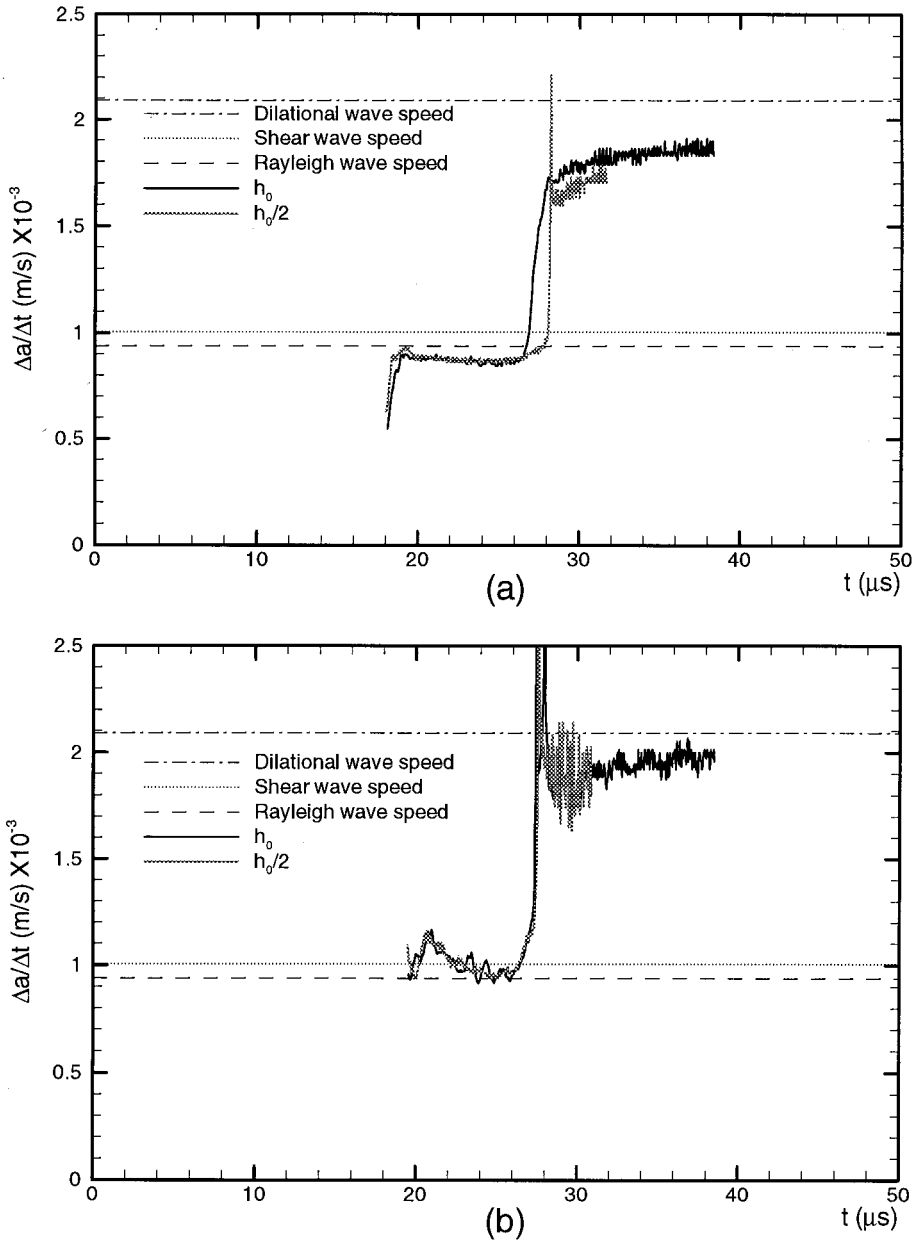

Fig. 14. Curves of crack speed, $\Delta a/\Delta t$ vs time, t, for two meshes. In one, denoted by h_0 the uniform grid spacing on the bond line is 75 μm, while in the other, denoted by $h_0/2$, this grid spacing is 37.5 μm. (a) $\sigma_{max}/\sigma^{PMMA} = 3/4$ and $V_1 = 30$ m/s. (b) $\sigma_{max}/\sigma^{PMMA} = 1/20$ and $V_1 = 5$ m/s.

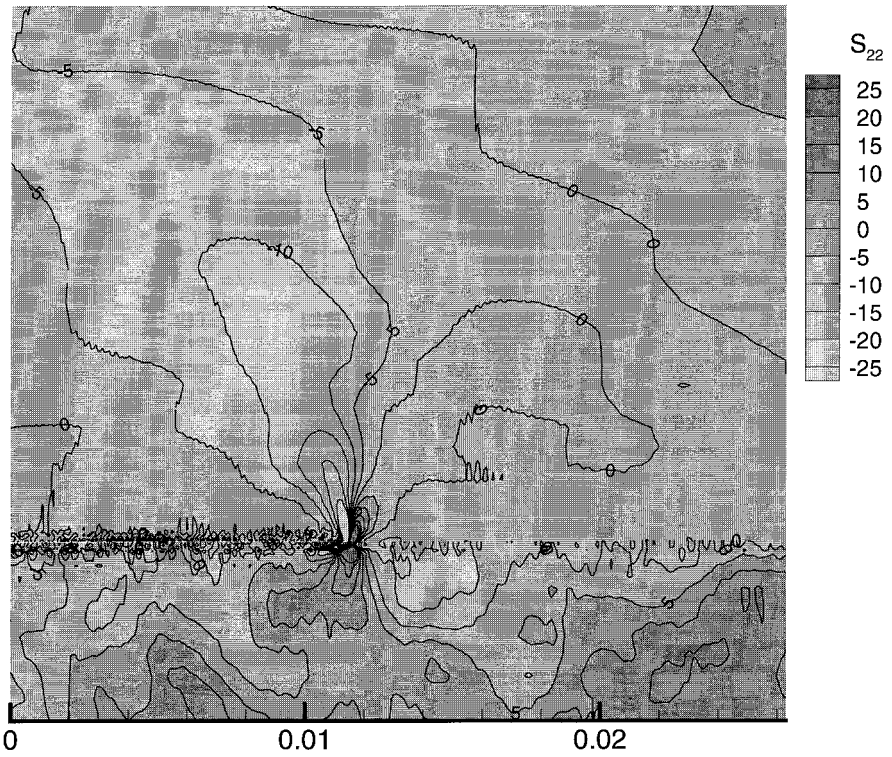

Fig. 15. Contours of the stress component S^{22} in the vicinity of the current crack tip at t = 40 μs, Δa = 11.9 mm and $\Delta a/\Delta t$ = 875 m/s for $V_1 = 10$ m/s and $\sigma_{\max} = 3\ \sigma^{\mathrm{PMMA}}/4$. Stress levels are in units of MPa and distances are in meters.

size as in Fig. 16(b). At t = 38 μs, micro-cracks have initiated in back of the shear crack (see Fig. 13). The small secondary stress concentration visible in Fig. 16(b) and (c) appears shortly after the crack tip speed reaches the Rayleigh wave speed of PMMA. As will be discussed in connection with Fig. 22, it moves with a constant speed approximately equal to the PMMA Rayleigh wave speed.

3.2. Comparison with experiment

Fig. 17 shows experimental crack speed vs time curves for aluminum-PMMA, Fig. 17(a), and for steel-PMMA, Fig. 17(b). The wave speeds for aluminum are nearly the same as for steel. The crack speed vs time response for the aluminum-PMMA system is similar to the behavior seen in Figs. 7 and 8, in that crack growth initiates shortly after the arrival of the first loading wave, progresses at a more or less constant crack speed which then increases rapidly when the reflected wave reaches the crack tip. However, in the experiment, in contrast to the

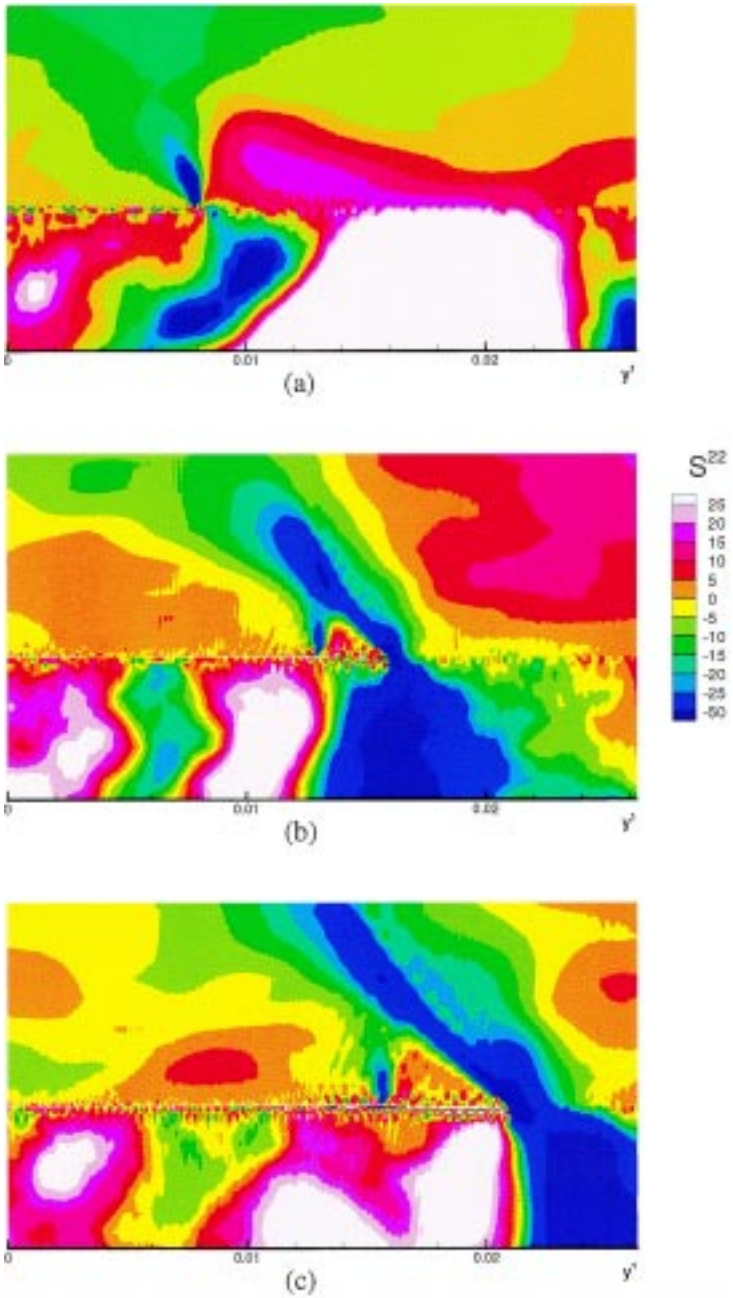

Fig. 16. Contours of the stress component S^{22} in the vicinity of the current crack tip for $V_1 = 20$ m/s and $\sigma_{max} = 3\ \sigma^{PMMA}/4$. Stress values are in units of MPa and distances are in meters. (a) t = 29 μs, Δa = 8.50 mm and $\Delta a/\Delta t$ = 1009 m/s. (b) t = 35 μs, Δa = 16.6 mm and $\Delta a/\Delta t$ = 1624 m/s. (c) t = 38 μs, Δa = 21.7 mm and $\Delta a/\Delta t$ = 1716 m/s.

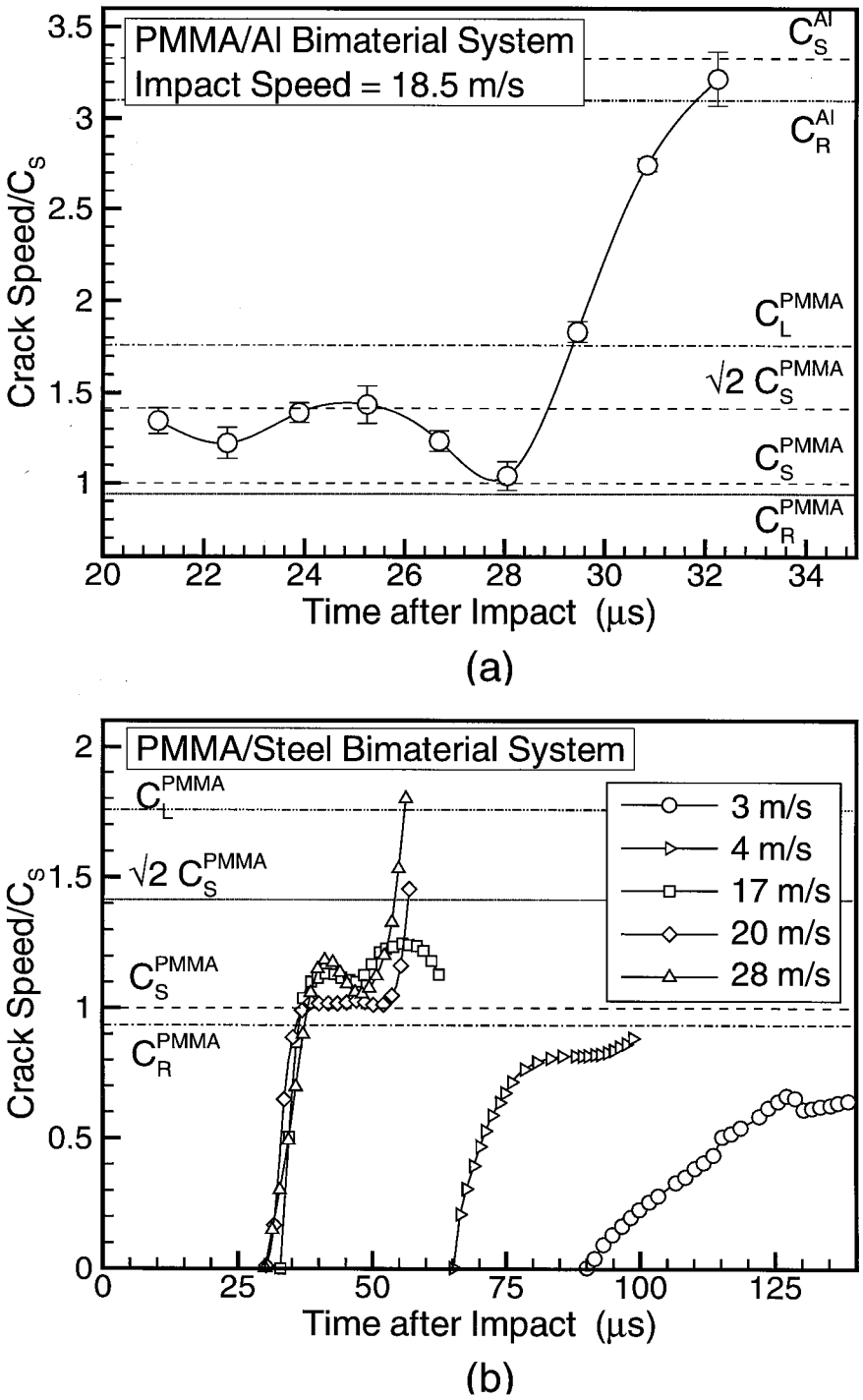

Fig. 17. Experimental curves of crack speed vs time. (a) Aluminum-PMMA. (b) Steel-PMMA.

simulations presented so far, the crack speed exceeds the PMMA Rayleigh wave speed before the arrival of the reflected wave and the crack speed eventually exceeds the dilational wave speed of PMMA and approaches the dilational wave speed of aluminum. For the steel-PMMA system, crack growth does not begin until the arrival of the reflected wave, but once crack growth begins the experimental crack speed histories are much like those in the simulations in Figs. 7 and 8.

This difference in initiation time can be related to the characterization of the cohesive properties of the bond. Fig. 18 shows results for computations where the characteristic lengths of the bond are increased by a factor of 10 to $\delta_n = 4.0$ μm and $\delta_t = 9.31$ μm. The bond line strength is $\sigma^{PMMA}/4$. For comparison purposes the crack speed history for the case with an impact velocity of 10 m/s, a bond line strength of $\sigma^{PMMA}/4$ and $\delta_n = 0.4$ μm, $\delta_t = 0.931$ μm is also shown. With the increased values of the characteristic lengths, which correspond to an increase in

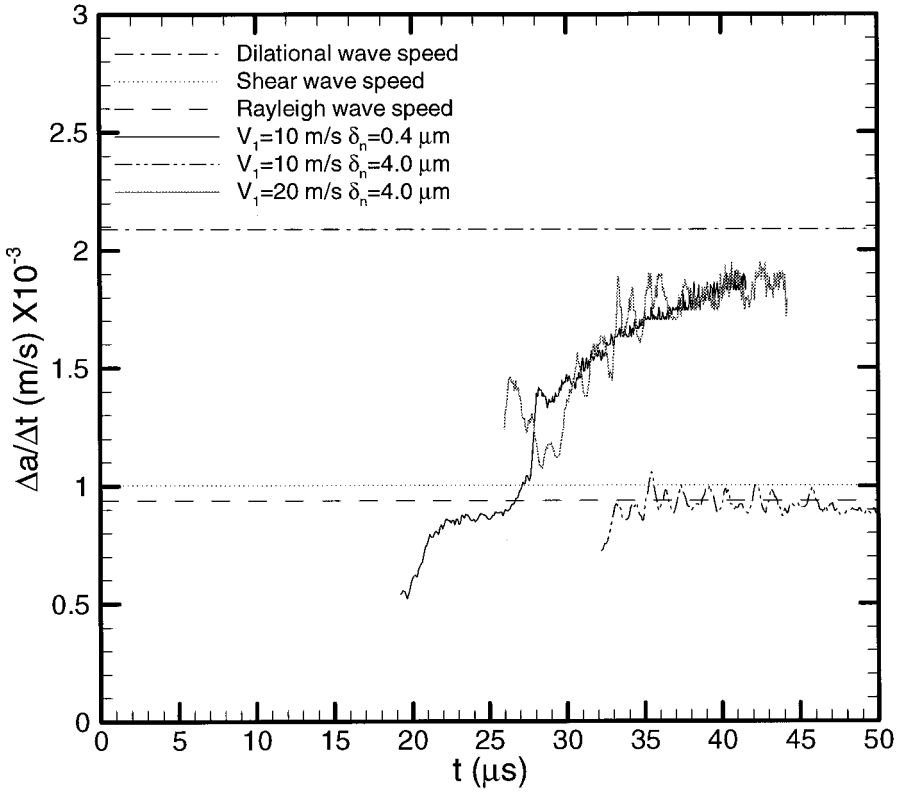

Fig. 18. Curves of crack speed, $\Delta a/\Delta t$ vs time, t, for $\delta_n = 4.0$ μm, $\delta_t = 9.31$ μm. The cohesive strength of the bond line is equal to $\sigma^{PMMA}/4$. For comparison purposes results are also shown for one calculation with $\delta_n = 0.4$ μm, $\delta_t = 0.931$ μm.

the work of separation with fixed cohesive strength, initiation is delayed until after the arrival of the reflected wave. The case with $V_1 = 20$ m/s gives rise to a local maximum crack speed followed by a local minimum crack speed, followed by a rapid rise in crack speed, as seen in the experimental results in Fig. 17(b). With $V_1 = 10$ m/s, initiation is further delayed as also seen in the experiments. However, despite the differences in initiation times, the crack speed for the case with $V_1 = 20$ m/s and $\delta_n = 4.0$ μm and that for the case with $V_1 = 10$ m/s and $\delta_n = 0.4$ μm are essentially the same for $t > 30$ μs.

Supersonic crack growth, i.e. crack speeds greater than the dilational wave speed of PMMA, is seen in Fig. 19. Here, $\sigma_{max} = \sigma^{PMMA}/4$ and $\delta_n = 0.4$ μm, but the impact speed is increased well beyond the value required for intersonic crack growth. For comparison purposes, the curve for $V_1 = 10$ m/s is repeated from Fig. 8. Increasing the impact velocity to 30 m/s or 40 m/s has little effect on the time at which crack growth initiates. However, the crack speed quickly rises to a value well above the PMMA shear wave speed but below the PMMA dilational wave

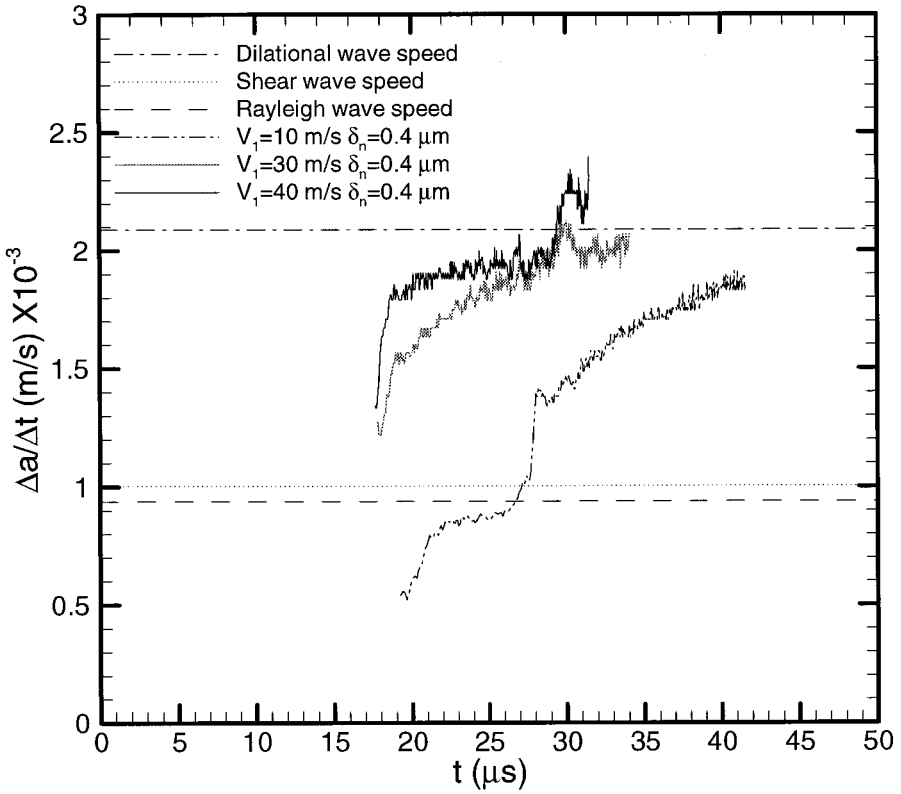

Fig. 19. Curves of crack speed, $\Delta a/\Delta t$ vs time, t, for various impact velocities. Here, $\delta_n = 0.4$ μm, $\delta_t = 0.931$ μm and the cohesive strength of the bond line is equal to $\sigma^{PMMA}/4$.

speed. When the reflected wave arrives at the crack tip, there is an increase in crack speed. With $V_1 = 30$ m/s the crack speed falls to a value just below the PMMA dilational wave speed, but with $V_1 = 40$ m/s the crack speed remains above the PMMA dilational wave speed. This behavior is similar to what was found in Figs. 7 and 8 for crack speeds that exceed the PMMA Rayleigh wave speed and indicates that there is a similar transition impact velocity required to exceed the PMMA dilational wave speed.

Fig. 20 is a selected sequence of four photoelasticity fringe patterns of interfacial crack growth along a Homalite-aluminum interface (because Homalite is a bifringent material whereas PMMA is not) from Samundrala and Rosakis (1998). The interface is horizontal and lies in the bottom of each image with the transparent Homalite half above while the opaque aluminum half lies below, outside the field of view. The interfacial crack moves from left to right, with the instantaneous crack tip speeds noted in the corner of each image. The time given in microseconds is measured from the time of impact. The region of contact behind the intersonically moving crack tip can be observed as the length over which the front and rear fringes converge to the interface. It is apparent that fundamental changes in the fringe patterns occur with increasing velocity. Whereas in the first two images where the crack speeds are 0.8 c_s^{Homalite} and 0.9 c_s^{Homalite}, respectively, the fringes converge smoothly to the interface, forming well-defined lobes, the fringes in the latter images become increasingly compressed and more complex, featuring two distinct shear shock waves emanating from the crack tip and from the end of a well formed contact zone, see Lambros and Rosakis (1995c), Singh et al. (1997) and Huang et al. (1998) for discussion.

For comparison with these experimental results, Figs. 21 and 22 show contours of the difference between the maximum (σ_1) and minimum (σ_2) in-plane principal stress values. In photoelasticity measurements using monochromatic light

$$N \propto (\sigma_1 - \sigma_2) \tag{13}$$

where N is the number of fringes.

Fig. 21 shows contours for $V_1 = 10$ m/s and $\sigma_{\max}/\sigma^{\text{PMMA}} = 3/4$ at $t = 40$ μs. Here, the crack speed is 875 m/s which is 0.87 c_s^{PMMA}. The values of $(\sigma_1 - \sigma_2)$ are positive because the minimum principal stress, σ_2, is negative and larger in absolute value than σ_1. The highest values of $(\sigma_1 - \sigma_2)$ are ahead of and behind the crack tip with much lower values above the crack.

Corresponding contours for $V_1 = 20$ m/s and $\sigma_{\max}/\sigma^{\text{PMMA}} = 3/4$ at the same three times as in Fig. 16 are shown in Fig. 22. At $t = 29$ μs in Fig. 22(a) where the crack speed is $\approx c_s^{\text{PMMA}}$, the contours near the crack tip are very similar to those in Fig. 21 and are also qualitatively similar to the first two of the experimental photoelastic fringe patterns in Fig. 20. At the higher crack speeds in Fig. 22(b) and (c), the low valued contours now protrude down to the bond line. This leads to two separated regions of high $(\sigma_1 - \sigma_2)$ near the bond line as can be seen clearly in Fig. 22(c). Again, the numerically obtained contours are remarkably similar to the latter two of the photoelastic fringe patterns, both

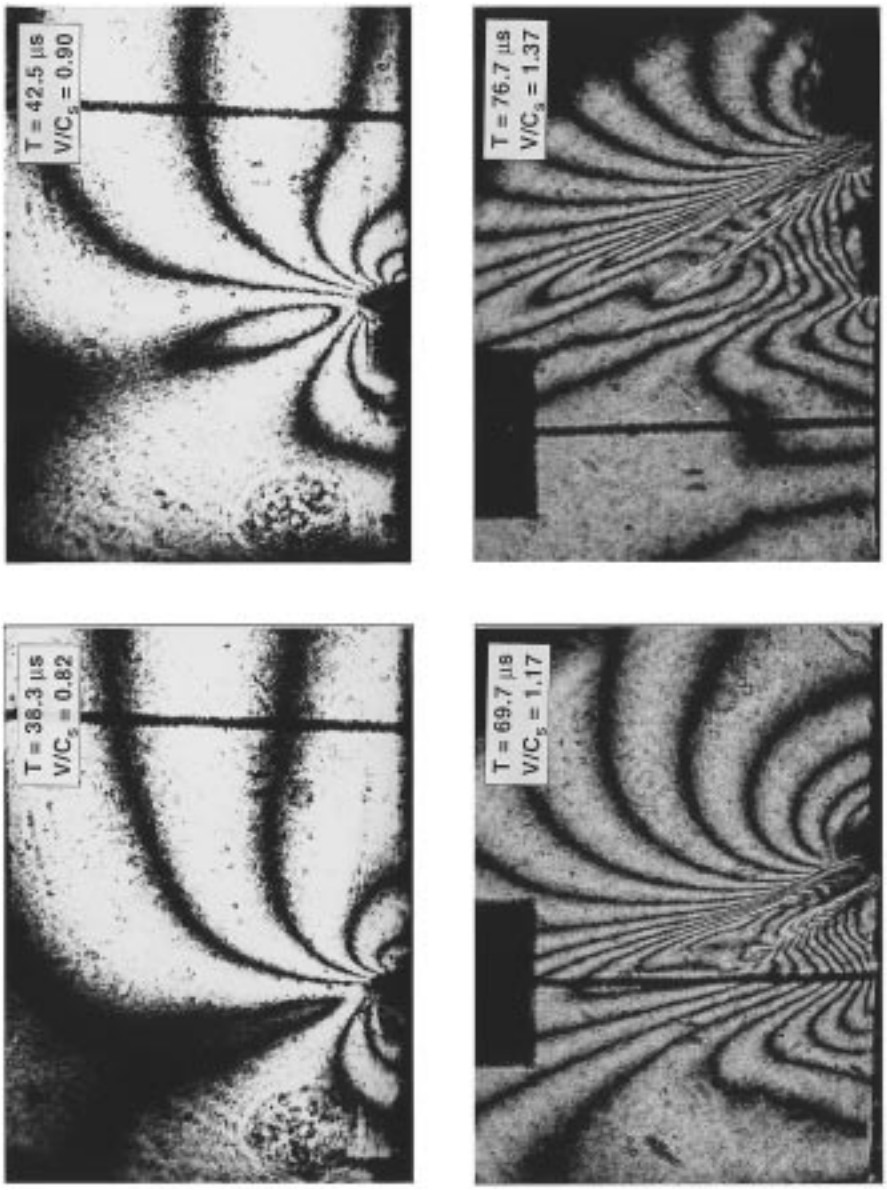

Fig. 20. Sequence of high speed isochromatic fringe patterns of bimaterial decohesion along a Homalite-aluminum interface, from Samundrala and Rosakis (1998). Here, v is the crack speed and c_s is the Homalite shear wave speed.

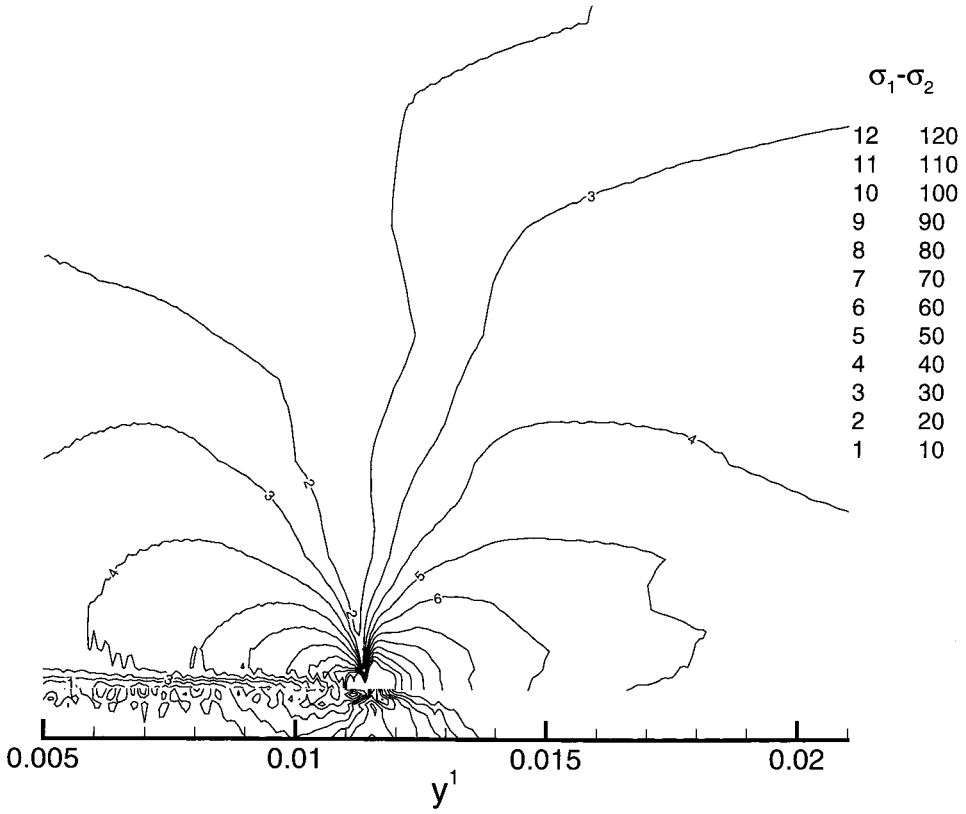

Fig. 21. Contours of the difference between the maximum (σ_1) and minimum (σ_2) in-plane principal stresses at $t = 40$ μs, $\Delta a = 11.9$ mm and $\Delta a/\Delta t = 875$ m/s for $V_1 = 10$ m/s and $\sigma_{max} = 3\ \sigma^{PMMA}/4$. Stress values are in units of MPa and distances are in meters.

featuring distinct shock wave like fringe concentrations emitting approximately from the location of the main crack tip. The intersection of high ($\sigma_1 - \sigma_2$) values with the bond line provides another measure of the crack location. This gives the crack location as being at 15.8 mm in Fig. 22(b) and at 20.8 mm in (c). Thus, with this definition of crack location the crack speed between Fig. 22(b) and (c) is 1667 m/s (1.66 c_s^{PMMA}). By way of comparison, the average of the instantaneous crack speeds, using Δ_t to define the crack location, in Fig. 22(b) and (c) is 1670 m/s. Although the average crack speeds are essentially the same, the crack location does depend on the measure used to define it. For example, in Fig. 22(b), using $\Delta_t = 5\ \delta_t$ to define the crack location gives $\Delta a = 16.6$ mm, using $\Delta_n = 5\ \delta_n$ to define the crack location gives $\Delta a = 16.4$ mm, and using intersection of high ($\sigma_1 - \sigma_2$) values with the bond line gives $\Delta a = 15.8$ mm. Corresponding values for Fig. 22(c) are $\Delta a = 21.7$ mm, $\Delta a = 21.4$ mm and $\Delta a = 20.8$ mm, respectively.

Another feature of note in the contours in Fig. 22(b) and (c) is the high

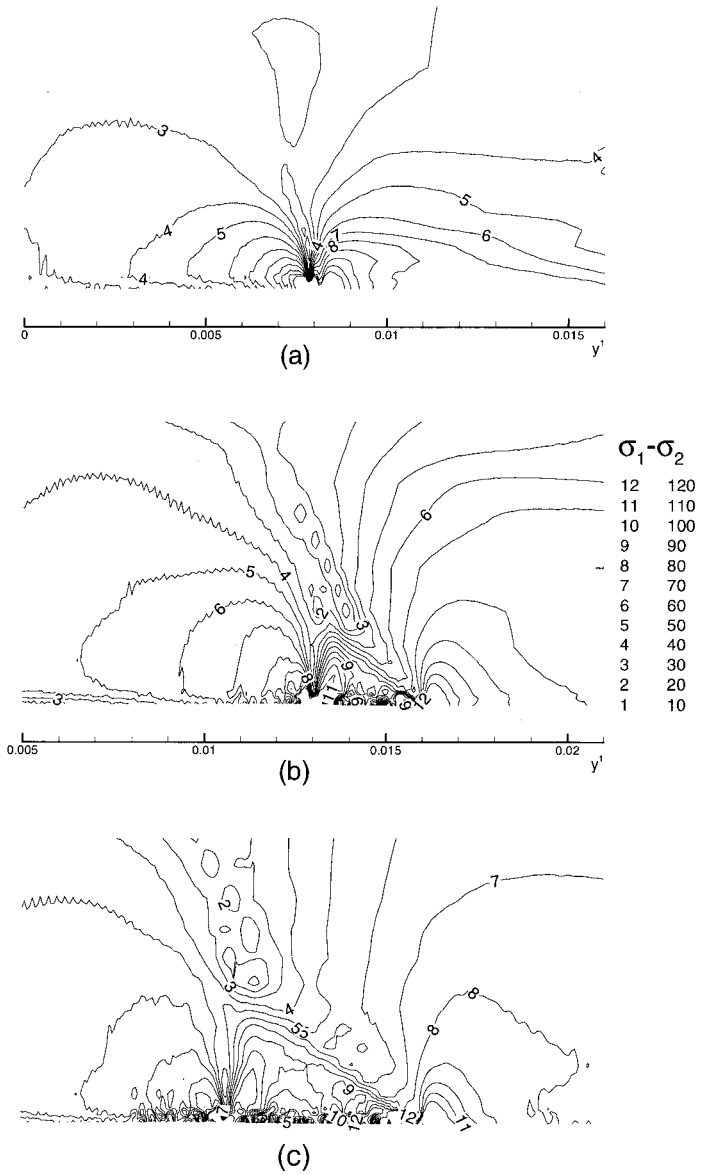

Fig. 22. Contours of the difference between the maximum (σ_1) and minimum (σ_2) in-plane principal stresses for $V_1 = 20$ m/s and $\sigma_{\max} = 3\,\sigma^{\mathrm{PMMA}}/4$. Stress values are in units of MPa and distances are in meters. (a) $t = 29$ μs, $\Delta a = 8.50$ mm and $\Delta a/\Delta t = 1009$ m/s. (b) $t = 35$ μs, $\Delta a = 16.6$ mm and $\Delta a/\Delta t = 1624$ m/s. (c) $t = 38$ μs, $\Delta a = 21.7$ mm and $\Delta a/\Delta t = 1716$ m/s.

gradient region that does not quite reach the crack surface at $y^1 = 0.013$ m in Fig. 22(b) and at $y^1 = 0.0156$ m in (c). The average speed of this feature between Fig. 22(b) and (c) is ≈ 870 m/s, which is within 8% of the PMMA Rayleigh wave speed. This Rayleigh type pulse is visible in Fig. 16(b) and (c), and was discussed in Section 3.1. This disturbance was first observed by Singh and Shukla (1996) and was found to trail the accelerating crack tip at an ever increasing distance in a manner that is very similar to what is observed in Fig. 16(b), (c), 22(b) and (c). It is also clearly visible in the third and fourth of the photoelastic fringe patterns in Fig. 20 (crack speeds of 1.17 and 1.37 times the Homalite shear wave speed, respectively).

4. Discussion

Dynamic crack growth along a steel-PMMA interface has been analyzed using a cohesive surface framework where the crack growth history is a direct outcome of the analysis, determined by the cohesive properties of the bond line (mainly the strength and the work of separation), by the material properties and by the imposed loading. A material length scale enters the formulation through the cohesive surface characteristic length. The configuration analyzed models that used in the experiments of Rosakis and co-workers, Lambros and Rosakis (1995a,b,c), Singh et al. (1997), where the crack is subject primarily to shear loading. Plane strain conditions are assumed and the crack is constrained to grow along the bond line.

The crack speed history is found to depend sensitively on the impact velocity. For a sufficiently low impact velocity, the crack speed increases smoothly to the Rayleigh wave speed of the more compliant material (PMMA). Above a sharply defined transition impact velocity, the crack speed increases to a value $\approx 10\%$ less than the PMMA dilational wave speed. The impact speed for this transition depends on the cohesive properties of the bond. However, the more or less steady-state crack speeds that are attained are independent of the bond cohesive properties or only weakly dependent on them. The calculations in Fig. 19 indicate that for a significantly higher impact velocity, the crack speed may exceed all characteristic wave speeds of the more compliant material.

The picture that emerges is that crack growth at a more or less constant speed can only take place at discrete crack speeds. These crack speeds are separated by 'barriers' and sufficient energy must be imparted to the crack process zone to overcome one of these 'barriers' and attain the next highest available crack speed. The first such 'barrier' is the one for the initiation of crack growth; the next is the Rayleigh wave speed of the more compliant material and the third is the dilational wave speed of the more compliant material. There may be others, but achieving higher crack speeds here was limited by the initiation and growth of a crack at the bond line near the impact surface.

This behavior is suggestive of the 'forbidden band' of crack speeds found by Marder and Gross (1995) in their lattice dynamics analysis of steady-state crack

growth in homogeneous solids. The 'forbidden band' of crack speeds in Marder and Gross (1995) is subsonic (between zero and about one quarter of the shear wave speed). Broberg (1989) has discussed forbidden crack speeds for homogeneous solids in the intersonic regime. Because of the tendency for crack branching in homogeneous solids, crack growth along relatively weak bimaterial interfaces may provide a more suitable system for investigating the phenomenon of discrete crack speeds.

Recently, Boudet and Ciliberto (1998) have reported on reflected ultrasound signals accelerating crack tips to reach a new crack speed plateau. A threshold is found in that a minimum amplitude of the acoustic signal is needed to change the crack speed. An analogous phenomenon occurs here with the reflected wave, instead of a superposed acoustic signal, providing the impetus for the crack speed to jump to the next available value. Presumably, another source of energy input, such as an acoustic wave, would have a similar effect.

Associated with the strong mode mixity of dynamic interface crack tip fields is contact of the crack faces, Lambros and Rosakis (1995c), Liu et al. (1995) and Huang et al. (1998). As seen in Fig. 13, multiple crack face contact develops which corresponds to micro-crack like openings separating multiple contact regions trailing behind the main shear crack. In the calculations, all material dissipation is neglected as is any dissipation associated with separation of the cohesive surfaces. The friction between contacting crack faces is ignored. Also, the actual contact conditions between the opposing crack faces is not accounted for; contact in the computations here just corresponds to a compressive normal traction. Furthermore, with the discretization used here there are only two or three points per half wave length of the oscillating opening displacement so that is not fully resolved. Nevertheless, the results here clearly show the tendency for large scale contact and micro-crack nucleation accompanying intersonic interface crack growth. It should be emphasized that this contact occurs on a much larger scale than that associated with the oscillating singularity for stationary and subsonic interface cracks, Rice (1988), Liu et al. (1993).

The comparison for two meshes in Fig. 14 shows that the overall features of the crack speed history do not change when the mesh resolution is increased by a factor of two. This does not mean, however, that the discretizations used are fine enough to resolve local features. The example of the repeated contacts in front of the crack tip in Fig. 13 has already been cited. In addition, the shock wave that develops when the crack speed exceeds the PMMA shear wave speed is not nearly as well represented as in the calculations of Xu and Needleman (1996). The numerical method used cannot resolve shock waves but with increased mesh resolution very high gradients in the vicinity of the crack tip can be resolved, at the expense, of course, of greatly increased computation times. It is not expected that improved resolution will change the qualitative features of the crack speed histories obtained here.

Liu et al. (1993), Liu et al. (1995) and Huang et al. (1998) have presented asymptotic crack tip fields for an isotropic elastic solid bonded to a rigid substrate, with the crack speed above the Rayleigh wave speed of the elastic solid.

Their analysis predicts a singularity with exponent less than 1/2 for crack speeds greater than the shear wave speed. As a consequence of the order of the singularity being less than 1/2, the energy release rate is zero. In the computations the work of separation for the cohesive surface is independent of the mode of crack opening and of the crack speed so that the energy required for separation must be reaching the bond line. A plot of the energy-flux vector near the crack tip location (not shown here) shows that energy flows into the bond line from the steel side and away from the bond line on the PMMA side.

In this regard, it worth recalling that when the crack speed has increased to the value just below the PMMA dilational wave speed, that the micro-crack like oscillations in normal opening have formed. Also, for the case with $\sigma_{\max} = \sigma^{\mathrm{PMMA}}/20$ in Fig. 11(b), the normal opening is advancing at a slower speed than the tangential separation. Hence, there is no longer a single crack-tip propagating at some constant speed, as assumed in the asymptotic analyses; a shear crack tip is found (defined by Δ_t reaching a specified value) that is ahead of the opening crack tip (defined by Δ_n reaching a specified value) when the crack speed exceeds the PMMA Rayleigh wave speed. When the crack speed is less than the PMMA Rayleigh wave speed these two crack tips are at the same location (see Fig. 13). One may speculate that a reason why the crack speed jumps to much above the PMMA Rayleigh wave speed is that in order for the crack to advance, it must advance fast enough for the structure of a single crack to break down. This picture is consistent with results of Andrews (1976) who carried out a finite difference solution for a plane strain shear crack in a homogeneous elastic solid using a slip-weakening model which, like in the cohesive surface formulation used here, involves specification of a traction-displacement jump constitutive relation. Andrews (1976) finds a transition from a crack running at the Rayleigh wave speed to one running about 15% slower than the dilational wave speed. Slip ahead of the main crack is found and Andrews (1976) notes the need for a smeared out rupture front when the crack has a finite fracture energy and propagates faster than the shear wave speed. Johnson (1990) has also found intersonic tip speeds in numerical simulations of slipping under mode II conditions using a slip-weakening model.

It should be noted at this point that the observation of areas of opening separating the regions of crack face contact behind the main shear crack tip are strongly reminiscent of dynamic rupture models introduced in seismology. In particular, the concept of a self healing pulse, see e.g. Weertman (1980), Heaton (1990), Andrews and Ben-Zion (1997) and Zheng and Rice (1998), has been used to study shallow crustal earthquakes and involves the dynamic propagation, along a weak fault line, of frictional shear cracks of finite length whose moving trailing edge is followed by frictional locking. Given the lack of friction in the calculations here the analogy is not complete. Nevertheless, it seems clear that when dynamic cracks become intersonic a complicated mechanism of multi-site contact favors the formation of such pulse like entities even in the absence of the huge static pressures that are present in the earth's environment.

The calculations here have at least qualitatively reproduced the sort of crack

speed histories seen in the experiments. The results show the key role played by wave reflections in the observed changes in crack speed. Crack initiation is found to occur somewhat after a loading wave reaches the crack tip. Whether this is the initial loading wave or a subsequent reflection depends, for a given cohesive strength, on the value of the cohesive characteristic length; larger characteristic lengths give rise to later crack growth initiation. The local stress fields in Figs. 21 and 22 have many features in common with the experimental fringe patterns in Fig. 20. Obtaining quantitative agreement between calculation and experiment will require an accurate representation of the cohesive surface constitutive response, including the characterization of frictional contact. Also, the calculations are based on a two dimensional plane strain framework and quantitative agreement may require full three dimensional analyses. In addition, it should be noted that the constant velocity prescribed as a boundary condition to the metal side in the numerical simulations only approximates the complex impact phenomena that occur in the experiments between the cylindrical steel projectile and the thin metal plate. At short times after impact the amplitude of the velocity should be approximately equal to half the projectile speed (which is measured in the experiments). At longer times, depending on the impedance mismatch between projectile and plate, this fraction may approach unity.

The analyses here, carried out within a cohesive surface fracture framework, have captured a variety of interface crack growth phenomena, including the prediction of crack speed histories that allow for intersonic crack growth, shear and opening crack tips that travel at different speeds, and micro-crack initiation on the bond line in front of the main opening crack and behind the shear crack tip. Such phenomena would be difficult, if not impossible, to predict using a traditional fracture mechanics formulation, i.e. one where a critical value of some measure of the amplitude of a crack tip singular field is used to predict crack growth.

Acknowledgements

A.N. is grateful for support from Sandia Corporation through grant LG-3057. A.J.R. acknowledges the support of the Office of Naval Research under Grant No. N00014-95-10453 to the California Institute of Technology and also the support of the National Science Foundation through Grant No. CMS-9424113. The computations reported on here were carried out on the Cray C90 at the Pittsburgh Supercomputer Center and on the Cray T90 at the San Diego Supercomputer Center.

References

Aleksandrov, V.M., Smetanin, B.I., 1990. Supersonic cleavage of an elastic strip. PMM USSR 54, 677–682.

Andrews, D.J., 1976. Rupture velocity of plane strain shear cracks. J. Geophys. Res. 81, 5679–5687.
Andrews, D.J., Ben-Zion, Y., 1997. Wrinkle-like slip pulse on a fault between different materials. J. Geophys. Res. 102, 553–571.
Archuleta, R.J., 1982. Analysis of near-source static and dynamic measurements from the 1979 Imperial Valley earthquake. Bull. Seismological Soc. Am. 72, 1927–1956.
Belytschko, T., Chiapetta, R.L., Bartel, H.D., 1976. Efficient large scale non-linear transient analysis by finite elements. Int. J. Numer. Meth. Engr. 10, 579–596.
Boudet, J.F., Ciliberto, S., 1998. Interaction of sound with fast crack propagation. Phys. Rev. Lett. 80, 341–344.
Broberg, K.B., 1960. The propagation of a Griffith crack. Ark. Fys. 18, 159.
Broberg, K.B., 1985. Irregularities at earth-quake slip. J. Tech. Phys. 26, 275–284.
Broberg, K.B., 1989. The near-tip field at high crack velocities. Int. J. Fract. 39, 1–13.
Burridge, R., 1973. Admissible speeds for plane-strain shear cracks with friction by lacking cohesion. Geophys. J. Roy. Soc. Lond. 35, 439–455.
Burridge, R., Conn, G., Freund, L.B., 1979. The stability of a rapid mode II shear crack with finite cohesive traction. J. Geophys. Res. 85, 2210–2222.
Bykovtsev, A.S., Kramarovskii, D.B., 1989. Non-stationary supersonic motion of a complex discontinuity. PMM USSR 53, 779–786.
Curran, D.R., Shockey, D.A., Winkler, S., 1970. Crack propagation at supersonic velocities, II. Theoretical model. Int. J. Fract. 6, 271–278.
Deng, X., 1993. General crack tip fields for stationary and steadily growing interface cracks in anisotropic bimaterials. J. Appl. Mech. 60, 183–189.
Freund, L.B., 1979. The mechanics of dynamic shear crack propagation. J. Geophys. Res. 84, 2199–2209.
Freund, L.B., 1990. Dynamic Fracture Mechanics. Cambridge University Press, Cambridge.
Georgiadis, H.G., 1986. On the stress singularity in transonic shear crack propagation. Int. J. Fract. 30, 175–180.
Heaton, T.H., 1990. Evidence for and implications of self-healing pulses of slip in earthquake rupture. Phys. Earth. Planet. Inter. 64, 1–20.
Huang, Y., Wang, W., Liu, C., Rosakis, A.J., 1998. Intersonic interfacial crack growth in a bimaterial: An investigation of crack face contact. J. Mech. Phys. Solids 46, 2233–2259.
Johnson, E., 1990. On the initiation of unidirectional slip. Geophys. J. Int. 101, 125–132.
Krieg, R.O., Key, S.W., 1973. Transient shell response by numerical time integration. Int. J. Numer. Meths. Engrg. 7, 273–286.
Lambros, J., Rosakis, A.J., 1995a. Dynamic decohesion of bimaterials: Experimental observations and failure criteria. Int. J. Solids Struct. 32, 2677–2702.
Lambros, J., Rosakis, A.J., 1995b. On the development of a dynamic decohesion criterion for bimaterials. Proc. R. Soc. Lond. A451, 711–736.
Lambros, J., Rosakis, A.J., 1995c. Shear dominated transonic interfacial crack growth in a bimaterial-I. Experimental observations. J. Mech. Phys. Solids 43, 169–188.
Liu, C., Huang, Y., Rosakis, A.J., 1995. Shear dominated transonic interfacial crack growth in a bimaterial-II. Asymptotic fields and favorable velocity regimes. J. Mech. Phys. Solids 43, 189–206.
Liu, C., Lambros, J., Rosakis, A., 1993. Highly transient elasto-dynamic crack growth in a bimaterial interface: higher order asymptotic analysis and optical experiment. J. Mech. Phys. Solids 41, 1887–1954.
Lo, C.Y., Nakamura, T., Kushner, A., 1994. Computational analysis of dynamic crack propagation along a bimaterial interface. Int. J. Solids Struct. 31, 145–168.
Marder, M., Gross, S., 1995. Origin of crack tip instabilities. J. Mech. Phys. Solids 43, 1–48.
Morrisey, J.W., Rice, J.R., 1998. Crack front waves. J. Mech. Phys. Solids 46, 467–488.
Nakamura, T., 1991. Three dimensional stress fields of elastic interface cracks. J. Appl. Mech. 58, 939–946.
Needleman, A., 1987. A continuum model for void nucleation by inclusion debonding. J. Appl. Mech. 54, 525–531.
Rice, J.R., 1988. Elastic fracture mechanics concepts for interfacial cracks. J. Appl. Mech. 55, 98–103.

Samundrala, O., Rosakis, A., 1998. Multiple crack face contact phenomena occurring during shear dominated intersonic and supersonic crack growth in bimaterials: Experiments and theory, in preparation.

Singh, R.P., Shukla, A., 1996. Subsonic and intersonic crack growth along a bimaterial interface. J. Appl. Mech. 63, 919–924.

Singh, R.P., Lambros, J., Shukla, A., Rosakis, A., 1997. Investigation of the mechanics of intersonic crack propagation along a bimaterial interface using coherent gradient sensing and photoelasticity, Proc. Roy. Soc. Lond. A453, 2649–2667.

Tippur, H.V., Rosakis, A.J., 1991. Quasi-static and dynamic crack growth along bimaterial interfaces: A note on crack-tip field measurements using coherent gradient sensing. Expt. Mech. 31, 243–251.

Washabaugh, P.G., Knauss, W.G., 1994. A reconciliation of dynamic crack velocity and Rayleigh wave speed in isotropic brittle solids. Int. J. Fract. 65, 97–114.

Weertman, J., 1980. Unstable slippage across a fault that separates elastic media of different elastic constants. Geophys. J. Int. 85, 1455–1461.

Winkler, S., Shockey, D.A., Curran, D.R., 1970. Crack propagation at supersonic velocities, I. Int. J. Fract. 6, 151–158.

Xu, X-P., Needleman, A., 1993. Void nucleation by inclusion debonding in a crystal matrix. Modell. Simul. Mat. Sci. Engin. 1, 111–132.

Xu, X-P., Needleman, A., 1994. Numerical simulations of fast crack growth in brittle solids. J. Mech. Phys. Solids 42, 1397–1434.

Xu, X-P., Needleman, A., 1995. Numerical simulations of dynamic interfacial crack growth allowing for crack growth away from the bond line. Int. J. Fract. 74, 253–275.

Xu, X-P., Needleman, A., 1996. Numerical simulations of dynamic crack growth along an interface. Int. J. Fract. 74, 289–324.

Yang, W., Suo, Z., Shih, C.F., 1991. Mechanics of dynamic debonding. Proc. R. Soc. Lond. A433, 679–697.

Zheng, G., Rice, J.R. 1998 Conditions under which velocity-weakening friction allows a self-healing versus a crack-like mode of rupture, Bull. Seismological Soc. Am. 88, 1466–1483.